FREQUENCY-DOMAIN SELF-ADJOINT *S*-PARAMETER SENSITIVITY ANALYSIS FOR MICROWAVE DESIGN

FREQUENCY-DOMAIN SELF-ADJOINT *S*-PARAMETER SENSITIVITY ANALYSIS FOR MICROWAVE DESIGN

By

XIAYING ZHU, B. Eng.

A Thesis

Submitted to the School of Graduate Studies

in Partial Fulfillment of the Requirements

for the Degree

Master of Applied Science

McMaster University

MASTER OF APPLIED SCIENCE (2008) McMASTER UNIVERSITY
(Electrical and Computer Engineering) Hamilton, Ontario

TITLE: **FREQUENCY-DOMAIN SELF-ADJOINT *S*-PARAMETER SENSITIVITY ANALYSIS FOR MICROWAVE DESIGN**

AUTHOR: Xiaying Zhu
B. Eng. (Electrical Engineering, Xi'an Jiaotong University)

SUPERVISOR: Dr. Natalia K. Nikolova, Associate Professor
Department of Electrical and Computer Engineering
Dipl. Eng. (Technical University of Varna)
Ph.D. (University of Electro-Communication)
P. Eng. (Ontario)

NUMBER OF PAGES: xvi, 111

ABSTRACT

This thesis proposes a sensitivity solver for frequency-domain electromagnetic (EM) simulators based on volume methods such as the finite-element method (FEM). The proposed sensitivity solver computes *S*-parameter Jacobians directly from the field solutions available from the EM simulation. It exploits the computational efficiency of the self-adjoint sensitivity analysis (SASA) approach where only one EM simulation suffices to obtain both the responses and their gradients in the designable parameter space. The proposed sensitivity solver adopts the system equations of the finite-difference frequency-domain (FDFD) method.

There are three major advantages to this development: (1) the Jacobian computation is completely independent of the simulation engine, its grid and its system equations; (2) the implementation is straightforward and in the form of a post-processing algorithm operating on the exported field solutions; and (3) it is computationally very efficient—time requirements are negligible in comparison with conventional field-based optimization procedures utilizing Jacobians computed via response-level finite differences or parameter sweeps.

The accuracy and the efficiency of the proposed sensitivity solver are verified in the sensitivity analysis and the gradient-based optimization of filters and antennas. Compared to the finite-difference approximation, drastic reduction of the time required by the overall optimization process is achieved. All examples use a commercial finite-element simulator.

Suggestions for future research are provided.

ACKNOWLEDGMENTS

The author wishes to express her greatest appreciation to Dr. Natalia K. Nikolova for her expert supervision, strong encouragement, and patience during the years of study. What the author has learned will benefit her forever.

The author would like to acknowledge the collaboration with her colleagues Dr. Mohamed Bakr, Yunpeng Song, Arshad Hasib, Peipei Zhao, Reza Khalaj Amineh, Li Liu, and Aastha Trehan from the Computational Electromagnetics Laboratory in Electrical and Computer Engineering Department at McMaster University.

The author would also like to thank the Department of Electrical and Computer Engineering, McMaster University, for a Research Assistantship, Teaching Assistantship and Scholarship.

Last but not least, the author deeply thanks her parents, Chunrong Zhu and Meifang Jiang, her family and all her friends, for their love, encouragement and support.

CONTENTS

LIST OF FIGURES

LIST OF TABLES

LIST OF ACRONYMS

AVM	Adjoint Variable Method
CAD	Computer-aided-design
DSA	Design Sensitivity Analysis
DRA	Dielectric-resonator Antenna
EM	Electromagnetics
FD	Finite difference
FFD	Forward Finite Difference
FDFD	Finite-difference Frequency-domain
FDTD	Finite-difference Time-domain
FEM	Finite-element Method
MoM	Method of Moments
PDE	Partial Differential Equation
SASA	Self-adjoint Sensitivity Analysis
SQP	Sequential Quadratic Programming
TLM	Transmission-line Method

Chapter 1

INTRODUCTION

Full-wave electromagnetic (EM) analysis based on current computer-aided-design (CAD) software is time intensive to an extent, which often makes the microwave design cycle prohibitively slow. The overall microwave design process, including design optimization, statistical, yield and tolerance analyses, can be greatly accelerated if design sensitivity information is made available. The purpose of design sensitivity analysis (DSA) is to evaluate the gradients of the system responses in the designable parameter space.

There are two major techniques to evaluate the design sensitivity: the response-level finite-difference (FD) method and the adjoint variable method (AVM). FD method is easy to implement but requires at least N+1 full-wave analyses per design iteration, where N is the number of designable parameters. On the other hand, the AVM is known to be the most efficient approach to DSA, especially for problems of high complexity where the number of state variables is much greater than the number of the required response derivatives [1]-[3]. It is

because that AVM yields the responses and their sensitivities with respect to all designable parameters through two system analyses: of an original problem and an adjoint problem.

The first developments in the adjoint-based DSA of microwave structures have been formulated and referred to as adjoint network methods [4], [5], based on Tellegen's theory of circuit concepts [6], [7]. Later, a set of feasible AVM approaches for field-based EM analyses have been proposed, both in the time domain (the transmission-line method, TLM [8], and the finite-difference time-domain method, FDTD [9]) and in the frequency domain (the frequency-domain TLM [10], [11], the method of moments, MoM [12], and the finite-element method, FEM).

Due to the response-dependent excitation of the adjoint simulation, all traditional AVM approaches require modifications of the EM simulators to solve the adjoint simulation, which is not allowed for most commercial CAD packages. Akel and Webb, for the first time, pointed out that, in the case of the FEM with tetrahedral edge elements, the sensitivities of the *S*-parameters can be derived without an adjoint simulation [12]. Recently, a general approach, named self-adjoint sensitivity analysis (SASA) [13], [14], has been proposed for the sensitivity analysis of microwave network parameters both in the frequency domain and in the time domain. Contrary to the traditional AVM approaches, the adjoint simulation has been eliminated. Not only does this mean that only one original system analysis is sufficient to yield both the responses and their

sensitivities, but also the computation of the response sensitivities can be integrated easily with existing commercial simulators as a post-process.

However, in order to implement the frequency-domain SASA, the EM simulator must have certain features [13]. First, it must be able to export the system matrix and the field/current vector solution. Second, it must be able to allow some control over the mesh generation so that the mesh topology remains unchanged upon parameter perturbation. The first feature deserves more attention. Most commercial simulators do not provide access to the system matrix. Besides, even if the system matrix is accessible, it is typically very large, especially for practical high-frequency structures. Therefore, it is necessary to export the system matrix to the computer disk. As a result, the better performance of the SASA is largely offset by the long time to write/read the system matrix to/from the disk.

In this thesis, we propose and implement a novel self-adjoint sensitivity analysis approach for S-parameters based on the finite-difference frequency-domain (FDFD) method, named finite-difference frequency-domain self-adjoint sensitivity analysis (FDFD-SASA). The new sensitivity solver is independent from the simulator's discretization method, grid and system equations. It relies on its own central-node finite-difference grid and a sensitivity formula based on the FDFD equation for the electric field. The only requirement of the EM simulator is to perform the original system analysis and to export the electric field at the designated perturbation points. Therefore, our sensitivity solver can operate as a software plug-in for commercial EM simulators, which are based on volumetric

partial differential equations. We apply our sensitivity solver to gradient-based optimization of microwave components.

The author's contributions can be summarized as follows:

1) The development of an efficient sensitivity computation algorithm based on the finite-element method, i.e., FDFD-SASA [15], [16].
2) The implementation of the FDFD-SASA approach to the *S*-parameter sensitivity analysis for dielectric and infinitesimally thin metallic structures with the commercial EM solver Ansoft HFSS® [17], [18].
3) The application of the FDFD-SASA approach to microwave design with gradient-based optimization algorithms [19].

Chapter 2 briefly reviews the methodologies of the AVM and the SASA in the frequency domain. The sensitivity expression using the exact AVM and the approximate AVM is given, respectively. A computational overhead comparison between the AVM and the FD method is presented. We also introduce the general SASA formula based on the finite-element method.

Chapter 3 begins with the outline of the theory of the FDFD-SASA and the application of the central-node finite-difference grid. The implementations for dielectric and metallic structures (including infinitesimally thin metallic structures) are presented afterwards. The FDFD-SASA is validated by two examples: an *H*-plane dielectric-resonator filter and a dielectric-resonator antenna.

Chapter 4 applies the FDFD-SASA to microwave design optimization. The validation examples use the same structures as in Chapter 3. The convergence and time requirements of the FDFD-SASA and the FD method are compared.

The thesis concludes in Chapter 5 with suggestions for further research.

References

[1] D. G. Cacuci, *Sensitivity & Uncertainty Analysis, Volume 1: Theory*. Boca Raton, FL: Chaman & Hall/CRC, 2003.

[2] A. D. Belegundu and T. R. Chandrupatla, *Optimization Concepts and Applications in Engineering*. Upper Saddle River, NJ: Prentice-Hall, 1999.

[3] E. J. Haug, K. K. Choi, and V. Komkov, *Design Sensitivity Analysis of Structural Systems*. Orlando, FL: Academic, 1986.

[4] S. W. Director and R. A. Roher, "The generalized adjoint network and network sensitivities," *IEEE Trans. Circuit Theory*, vol. CT-16, pp. 318-323, Aug. 1969.

[5] S. W. Director and R. A. Rohrer, "Automated network design—The frequency-domain case," *IEEE Trans. Circuit Theory*, vol. CT-16, pp. 330-337, Aug. 1969.

[6] B. D. H. Tellegen, "A general network theorem with applications," *Philips Res. Rep.*, vol. 7, pp. 259-269, 1952.

[7] P. Penfield, Jr., R. Spence, and S. Duinker, "A generalized form of Tellegen's theorem," *IEEE Trans. Circuit Theory*, vol. CT-17, pp. 302-305, Aug. 1970.

[8] M. H. Bakr, N. K. Nikolova, "An adjoint variable method for time domain TLM with wide-band Johns matrix boundaries," *IEEE Trans. Microwave Theory Tech.,* vol. 52, pp. 678-685, Feb. 2004.

[9] N. K. Nikolova, H. W. Tam, M. H. Bakr, "Sensitivity analysis with the FDTD method on structured grids," *IEEE Trans. Microwave Theory Tech.,* vol. 52, pp. 1207-1216, Apr. 2004.

[10] M. H. Bakr and N. K. Nikolova, "An adjoint variable method for frequency domain TLM problems with conducting boundaries," *IEEE Microwave and Wireless Components Letters*, vol. 13, pp. 408-410, Sep. 2003.

[11] S. M. Ali, N. K. Nikolova, and M. H. Bakr, "Central adjoint variable method for sensitivity analysis with structured grid electromanetic solvers," *IEEE Trans. Magnetics,* vol. 40, pp. 1969-1971, Jul. 2004.

[12] H. Akel and J. P. Webb, "Design sensitivities for scattering-matrix calculation with tetrahedral edge elements," *IEEE Trans. Magnetics*, vol. 36, pp. 1043-1046, Jul. 2000.

[13] N. K. Nikolova, J. Zhu, D. Li, M. Bakr, and J. Bandler, "Sensitivities of network parameters with electromagnetic frequency domain simulators," *IEEE Trans. Microwave Theory Tech.*, vol. 54, pp. 670-681, Feb. 2006.

[14] N. K. Nikolova, Ying Li, Yan Li, and M. H. Bakr, "Sensitivity analysis of scattering parameters with electromagnetic time-domain simulators," *IEEE Trans. Microwave Theory Tech.*, vol. 54, pp. 1589-1610, Apr. 2006.

[15] X. Zhu, A. Hasib, and N. K. Nikolova, "Electromagnetic sensitivity analysis of scattering parameters based on the FDFD method," *Int. Symp. on Signals, Systems, and Electronics (ISSSE 2007)*, pp. 165-168, Jul.-Aug. 2007.

[16] N. K. Nikolova, A. Hasib, and X. Zhu, "Independent sensitivity solver based on the frequency domain finite difference method," *The 24th Int. Review of Progress in Applied Computational Electromagnetics (ACES 2008)*, pp. 1024-1029, Mar.-Apr. 2008.

[17] Ansoft HFSS ver. 10, Ansoft Corporation, 225 West Station Square Drive, Suite 200, Pittsburgh, PA 15219, USA, 2006, www.ansoft.com.

[18] Ansoft HFSS ver. 11, Ansoft Corporation, 225 West Station Square Drive, Suite 200, Pittsburgh, PA 15219, USA, 2007, www.ansoft.com.

[19] X. Zhu, A. Hasib, N.K. Nikolova, and M.H. Bakr, "Efficient electromagnetic optimization using self-adjoint Jacobian computation based on a central-node FDFD method," *IEEE MTT-S Int. Microwave Symposium*, pp. 979-982, Jun. 2008.

Chapter 2

METHODOLOGIES OF THE ADJOINT-VARIABLE AND THE SELF-ADJOINT SENSITIVITY ANALYSES

2.1 Introduction

Design sensitivity analysis (DSA) aims at finding the derivatives of the system responses with respect to designable parameters. Currently, commercial electromagnetic (EM) simulators do not provide sensitivity information. If sensitivities are required, a simple but inefficient finite-difference (FD) approximation at the response level is usually carried out, which requires at least one additional system analysis for each designable parameter. Preliminary parameter sweep is also used, but it is even more time-consuming than the FD approximation.

On the other hand, the adjoint variable method (AVM) requires at most one additional system analysis (adjoint system analysis) for all designable parameters. Compared to the FD approximation, the AVM is much more efficient especially when the number of designable parameters is large. However, the excitation of the adjoint system is response-dependent. Hence, modifications of the underlying EM numerical algorithm are required [1]. The self-adjoint sensitivity analysis (SASA) exploits the nature of the linear problem and eliminates the adjoint system analysis for certain objective functions, i.e., network parameters [2], [3].

In this chapter, the methodologies of the AVM [4] and the SASA [2], [3] are briefly reviewed. Section 2.2 introduces the AVM in the frequency domain. Section 2.3 presents the formulation for the SASA of *S*-parameters based on the finite-element method (FEM) [5].

2.2 Frequency-domain Adjoint Variable Method

2.2.1 Exact frequency-domain AVM [4]

After proper discretization, a time-harmonic linear EM problem—problem involving linear materials only—can be described as a linear system of complex equations [4], [6]:

$$\boldsymbol{A}\boldsymbol{x} = \boldsymbol{b}. \tag{2.1}$$

Here, the system matrix $\boldsymbol{A} \in \mathbb{C}^{M \times M}$ is a function of the vector of designable parameters $\boldsymbol{p}$, which contains N shape and/or material parameters. Thus, the vector of state variables $\boldsymbol{x} \in \mathbb{C}^{M \times 1}$ is an implicit function of $\boldsymbol{p}$. The right-hand side $\boldsymbol{b} \in \mathbb{C}^{M \times 1}$ results from the EM excitation and/or the inhomogeneous boundary conditions.

For the purposes of optimization, the overall system performance is often evaluated in terms of a single scalar real-valued objective function, which may be a function of complex responses, e.g., S-parameters. Here, we consider a single, possibly complex, function $f(\boldsymbol{x}, \boldsymbol{p})$. The goal of the sensitivity analysis is to determine the gradient of the objective function $f(\boldsymbol{x}, \boldsymbol{p})$ with respect to $\boldsymbol{p}$ at the field solution $\bar{\boldsymbol{x}}$ of (2.1)

$$\nabla_p f\left(\boldsymbol{p}, \bar{\boldsymbol{x}}(\boldsymbol{p})\right) \text{ subject to } \boldsymbol{A}\bar{\boldsymbol{x}} = \boldsymbol{b}. \tag{2.2}$$

Here, the gradient is defined as a row operator [6], [7]

$$\nabla_p f = \left[\frac{\partial f}{\partial p_1} \quad \frac{\partial f}{\partial p_2} \quad \cdots \quad \frac{\partial f}{\partial p_N} \right]. \tag{2.3}$$

Furthermore, we have

$$\nabla_p f = \nabla_p^e f + \nabla_p f \cdot \nabla_p \boldsymbol{x}. \tag{2.4}$$

$\nabla_p^e f$ represents the explicit dependence on $\boldsymbol{p}$. Explicit dependence arises when f depends on the field/current solution either at points whose coordinates are affected by the change of a shape parameter or at points whose constitutive

parameters are affected by the change of a material parameter [2]. $\nabla_p f \cdot \nabla_p \boldsymbol{x}$ reflects the fact that f is an implicit function of $\boldsymbol{p}$ through $\boldsymbol{x}$.

Applying the methodology of the adjoint sensitivity analysis of a linear complex system to (2.4) [4], [7], [8], the adjoint sensitivity expression can be obtained as

$$\nabla_p f = \nabla_p^e f + \hat{\boldsymbol{x}}^T \cdot \nabla_p \left(\boldsymbol{b} - \boldsymbol{A}\bar{\boldsymbol{x}} \right). \tag{2.5}$$

The adjoint-variable vector $\hat{\boldsymbol{x}}$ is the solution to the adjoint system

$$\boldsymbol{A}^T \cdot \hat{\boldsymbol{x}} = \left(\nabla_x f \right)_{x=\bar{x}}^T. \tag{2.6}$$

Here, the adjoint system excitation $\left(\nabla_x f \right)^T$ is a column of the derivatives with respect to each of the state variables evaluated at the current solution $\boldsymbol{x} = \bar{\boldsymbol{x}}$.

To investigate (2.5), we rewrite it as

$$\frac{\partial f}{\partial p_n} = \frac{\partial f^e}{\partial p_n} + \hat{\boldsymbol{x}}^T \cdot \left[\frac{\partial \boldsymbol{b}}{\partial p_n} - \frac{\partial \boldsymbol{A}}{\partial p_n} \cdot \bar{\boldsymbol{x}} \right], \; n = 1, 2, \ldots, N. \tag{2.7}$$

Equation (2.7) shows that three quantities are necessary to calculate the response derivatives: (1) the original solution $\bar{\boldsymbol{x}}$, (2) the adjoint solution $\hat{\boldsymbol{x}}$, and (3) the derivatives of the system matrix with respect to the designable parameters $\partial \boldsymbol{A} / \partial p_n$, $n = 1, 2, \ldots, N$. Complications arise with the system matrix generated by numerical methods using structured grids, such as the transmission line method (TLM), because it is not differentiable with respect to shape parameters [4], [6]. Even in the case when the derivatives of the system matrix exist, complicated pre-process is involved.

2.2.2 Approximate frequency-domain AVM for structured grids [6]

Instead of computing the derivatives of the system matrix analytically, finite-difference ratios are applied in (2.7). According to [6], one of two possible discrete AVM sensitivity expressions is described by (2.8) and (2.9)

$$\left(\frac{df}{dp_n}\right)_{\mathrm{I}} \approx \frac{\partial f^e}{\partial p_n} + \hat{\boldsymbol{x}}^T \cdot \left[\frac{\Delta \boldsymbol{b}}{\Delta p_n} - \frac{\Delta \boldsymbol{A}}{\Delta p_n} \cdot \bar{\boldsymbol{x}}_n\right], \quad n = 1,2,\ldots,N \tag{2.8}$$

$$\boldsymbol{A}^T \cdot \hat{\boldsymbol{x}} = \left(\nabla_x f\right)^T_{x=\bar{x}} . \tag{2.9}$$

Here, $\bar{\boldsymbol{x}}_n$ denotes the solution to the original system with a perturbation Δp_n. Thus, $\bar{\boldsymbol{x}}_n$ is parameter-dependent, which means that N additional system analyses are needed for N designable parameters. However, the parameter-dependent feature is overcome by a simple mapping technique [9] based on perturbation theory [10]. Instead of performing N perturbed original system analyses, all vectors $\bar{\boldsymbol{x}}_n$ $(n = 1,\ldots,N)$ can be obtained from the unperturbed system solution $\bar{\boldsymbol{x}}$ without any computational overhead.

An alternative to (2.8) and (2.9) is the sensitivity formula [6]

$$\left(\frac{df}{dp_n}\right)_{\mathrm{II}} \approx \frac{\partial f^e}{\partial p_n} + \hat{\boldsymbol{x}}_n^T \cdot \left[\frac{\Delta \boldsymbol{b}}{\Delta p_n} - \frac{\Delta \boldsymbol{A}}{\Delta p_n} \cdot \bar{\boldsymbol{x}}\right], \quad n = 1,2,\ldots,N \tag{2.10}$$

$$\boldsymbol{A}_n^T \cdot \hat{\boldsymbol{x}}_n = \left(\nabla_x f\right)^T_{x=\bar{x}} . \tag{2.11}$$

Here, $\hat{\boldsymbol{x}}_n$ is the solution to the adjoint system with a perturbation Δp_n, which can be obtained from the solution of the unperturbed adjoint system $\hat{\boldsymbol{x}}$ by a simple mapping. Hence, only one unperturbed adjoint analysis is needed.

The two discrete sensitivity expressions are theoretically equivalent. They both take the second-order terms into account and eliminate the derivatives of the system matrix. Hence, they are accurate and versatile. However, based on our previous experiences, we expect (2.10) to have less computational error especially for highly nonlinear responses [4], [6].

2.2.3 Computational overhead comparison between the AVM and the FD method

Regardless of the number of designable parameters, two system analyses—one of the original problem, the other of the adjoint problem—are sufficient for the adjoint sensitivity analysis. Each full-wave system analysis comprises two steps of computations. The first step is the matrix fill, while the second one is to solve the equation (2.1). For the adjoint system analysis, the system matrix is the transpose of the original one; therefore, a matrix fill is not required. The computational time required to transpose a matrix is negligible. Another main overhead of the AVM is the computation of the derivatives of the system matrix, which is equivalent to a matrix fill for each designable parameter.

The FD method implements the finite-difference approximation at the response level. In addition to the original full-wave system analysis, at least one additional system analysis is performed per designable parameter with a slight perturbation in this parameter.

The computational overhead comparison of the sensitivity analysis using the FD method and the AVM is shown in Table 2.1.

TABLE 2.1
COMPUTATIONAL OVERHEAD COMPARISON BETWEEN THE FD METHOD AND THE AVM

Method	Matrix fills	System solutions	Sensitivity formula computation
FD	N+1	N+1	0
AVM	N+1	2	N

In general, the time required by a matrix fill is far less than the time required by a system solution, especially for an electrically large problem. Also, the computation time of the sensitivity formula is negligible even compared with the matrix fill. Thus, the AVM is much more efficient, especially in an optimization process which typically requires hundreds of iterations.

2.3 Self-adjoint Sensitivity Analysis for *S*-Parameters

2.3.1 The finite-element method (FEM) [5]

The mathematical modeling of some physical systems can be categorized as boundary-value problems. Such problems are defined by a governing differential equation

$$\mathcal{L}\phi = f, \tag{2.12}$$

and the respective boundary conditions. Here, $\mathcal{L}$ is a differential operator, f is the excitation or forcing function, while ϕ is the unknown solution. In EM, the differential equation can either be the Poisson equation or the scalar/vector wave or Helmholtz equations. The boundary conditions may be the Dirichlet, Neumann, or mixed Dirichlet and Neumann conditions. Only very few problems, e.g., wave propagation in a regular waveguide, have analytical solutions to (2.12). Most practical engineering problems cannot be solved analytically.

The FEM is a numerical technique for obtaining approximate solutions to boundary-value problems. It was originally employed in structural analysis in the 1950s. So far, the method has been expansively developed and applied to a wide variety of engineering disciplines, such as mechanical engineering and electrical engineering. The adaptability to arbitrary geometry and material inhomogeneity, along with the relatively low memory requirement, has allowed the FEM to become one of the most popular numerical methods.

In the late 1960s, the FEM was first introduced to EM problems in waveguide and cavity analysis. Later, the successful applications to open domain problems in scattering, microwave circuits, and antennas came about, followed by the development of absorbing and matched-port boundary conditions. Today, the FEM has become a major numerical method in computational electromagnetics [11].

The implementation of the FEM consists of four steps: (1) discretization of the domain, (2) selection of the interpolation functions, (3) formulation of the system equations, and (4) solution of the system equations.

The principle of the FEM is to replace an entire continuous domain by a number of subdomains so that simple interpolation functions can be employed. Thus, the first step is perhaps the most important one because the discretization manner determines the accuracy of the numerical result, the computational time, and the computer memory. The entire domain is subdivided into a number of small domains, referred to as elements. Typically, one-, two-, and three-dimensional domains are approximated by short-line elements, triangular or rectangular elements, and tetrahedron or prisms bricks. The line element, the triangle and the tetrahedron are the basic ones.

The final formulation of the problem is set up in terms of the unknown function ϕ at nodes (scalar FEM) or edges (vector FEM) associated with the elements. A complete description of these nodes or edges is necessary, which includes the coordinate values, local indexes (indicating the positions within an element) and global indexes (indicating the positions in the entire system). The global index and the local index are related via one index table, as shown in figure 2.1 and table 2.2 for a two-dimensional example.

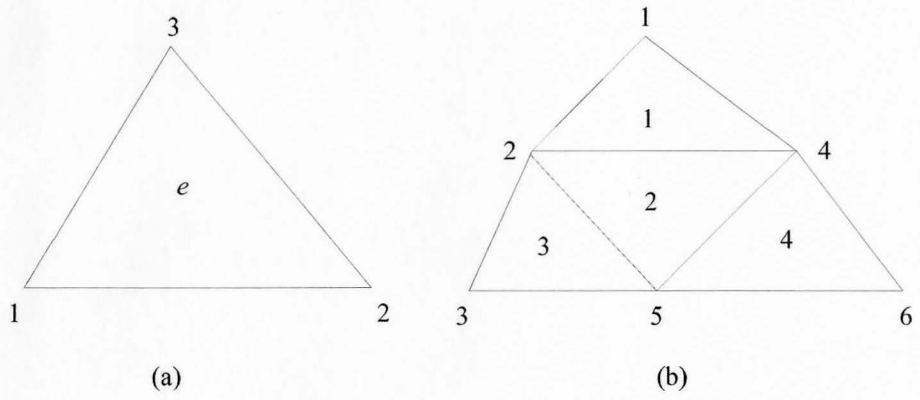

Figure 2.1 The index of the node: (a) local index; (b) global index.

TABLE 2.2
THE MAPPING TABLE BETWEEN THE LOCAL INDEX AND THE GLOBAL INDEX

i / *e*	1	2	3
1	2	4	1
2	5	4	2
3	3	5	2
4	5	6	4

The second step is the selection of an interpolation function, which can be a linear, quadratic, or higher-order polynomial. Applying the selected interpolation function with the values of the solution at elemental nodes, the unknown solution anywhere within an element can be estimated in the following form

$$\tilde{\phi}^e = \sum_{j=1}^{n} N_j^e \phi_j^e \,. \tag{2.13}$$

Here, n is the number of nodes in the element, ϕ_j^e is the value of ϕ at node j of the element, and N_j^e is the interpolation coefficient for node j. The highest order of the functions N_j^e determines the order of the element.

Both the Ritz variational and Galerkin methods can be used to formulate the system equations after the preceding steps. More mathematical details can be found in [5]. After imposing the boundary conditions, we can obtain the final system equations. One of the general matrix forms is as follows:

$$\boldsymbol{K}\boldsymbol{\varphi} = \boldsymbol{b} \,. \tag{2.14}$$

Equation (2.14) is equivalent to (2.1). $\boldsymbol{K}$ is an M by M system matrix where M is the number of nodes or edges. The application of the FEM leads to a sparse system matrix which can be stored with low memory requirement. $\boldsymbol{\varphi}$ is the solution to (2.14).

Another form arising in practical problems is

$$\boldsymbol{A}\boldsymbol{\varphi} = \lambda \boldsymbol{B}\boldsymbol{\varphi} \,. \tag{2.15}$$

Equation (2.15) is of the eigenvalue type, where $\boldsymbol{K}$ is substituted by $\boldsymbol{A} - \lambda \boldsymbol{B}$, while the excitation $\boldsymbol{b}$ vanishes.

2.3.2 SASA for *S*-parameters based on the FEM [2]

The AVM, which needs an adjoint system analysis with the response-

dependent adjoint excitation, is impractical when applied with most of the commercial of the EM simulators. Akel and Webb have pointed out that the sensitivity of the *S*-matrix can be derived without an adjoint system analysis based on the FEM with tetrahedral edge elements [12]. For a linear EM problem, a new approach, the self-adjoint sensitivity analysis, can eliminate the adjoint system analysis for network parameters. Here, we only show a simple derivation of the SASA for *S*-parameters based on the FEM method. The more detailed explanation can be found in [2].

Reconsider (2.10), when f is an *S*-parameter. Then, both $\partial f^e/\partial p_n$ and $\Delta \boldsymbol{b}/\Delta p_n$ vanish. It is because network parameters are computed from the solution at the ports whose shape and materials do not change. Besides, the energy launching at the ports does not change either. Equation (2.10) reduces to

$$\frac{df}{dp_n} \approx -\hat{\boldsymbol{x}}_n^T \cdot \frac{\Delta \boldsymbol{A}}{\Delta p_n} \cdot \bar{\boldsymbol{x}},\ n = 1,2,\ldots,N\,. \tag{2.16}$$

$\hat{\boldsymbol{x}}_n^T$ is defined in (2.11), and can be obtained by solving (2.9) and using the mapping technique.

For a *K*-port structure, in order to obtain the full scattering matrix for a particular mode, K solutions of (2.1) are carried out with one of the ports being excited while the rest of the ports are matched. We assume that the jth port is excited and consider S_{kj}, $k, j = 1,2,\ldots,K$, as the response of interest f [see (2.16)]. According to [2], we have

$$\left(\nabla_{\boldsymbol{x}} S_{kj}\right)^T = \frac{1}{2\gamma_k E_{0k} \iint\limits_{j\text{-port}} (\mathbf{a}_n \times \mathbf{E}_j^{\text{inc}}) \cdot (\mathbf{a}_n \times \mathbf{e}_j) ds_j} \cdot \boldsymbol{b}_k . \tag{2.17}$$

Here, γ_k is the modal propagation constant of the kth port, E_{0k} is the incident field magnitude at the kth port, $\mathbf{E}_j^{\text{inc}}$ is the incident field solution at the jth port, $\mathbf{e}_j$ is the normalized modal vector at the jth port and $\mathbf{a}_n$ is the unit normal to the respective port surface. We note that the FEM system matrix $\boldsymbol{A}$ is symmetric [5]

$$\boldsymbol{A} = \boldsymbol{A}^T . \tag{2.18}$$

From (2.17) and (2.18), the adjoint solution $\hat{\boldsymbol{x}}_{kj}$ of (2.9) can be derived from the original solution $\boldsymbol{x}_k$ by a simple multiplication with a complex constant κ_{kj}, which is called the self-adjoint constant

$$\hat{\boldsymbol{x}}_{kj} = \kappa_{kj} \cdot \boldsymbol{x}_k \tag{2.19}$$

$$\kappa_{kj} = \frac{1}{2\gamma_k E_{0k} \iint\limits_{j\text{-port}} (\mathbf{a}_n \times \mathbf{E}_j^{inc}) \cdot (\mathbf{a}_n \times \mathbf{e}_j) ds_j} . \tag{2.20}$$

To summarize the above theory, we have

$$\frac{dS_{kj}}{dp_n} \approx -\kappa_{kj} \left[\left(\bar{\boldsymbol{x}}_k \right)_n \right]^T \cdot \frac{\Delta \boldsymbol{A}}{\Delta p_n} \cdot \bar{\boldsymbol{x}}_j, \; n = 1, 2, \ldots, N, \; k, j = 1, 2, \ldots, K . \tag{2.21}$$

SASA requires the field solutions only from the original system analysis to compute the derivatives of the whole scattering matrix with respect to all designable parameters. Compared to the traditional AVM, SASA not only improves the efficiency but also eliminates the necessity of modifying the EM

simulators in order to perform adjoint analyses.

To implement (2.21), an EM simulator must have three features: (1) it must be able to export the system matrix so that the user can compute the system matrix derivatives; (2) it must allow the user some control over the mesh generation to make sure the dimension of the system matrix does not change after the perturbation; and (3) it must be able to export the field solution $\bar{x}$ as in (2.21). The second and third features are available to most EM simulators. But the first feature deserves more attention. Most commercial simulators do not give access to the system matrix. Even if they do, it is necessary to export the system matrix to the computer disk. Since the system matrix is usually very large, it takes long time to write and read the system matrix, which offsets the better performance of the SASA.

2.4 References

[1] N. K. Nikolova, H. W. Tam, M. H. Bakr, "Sensitivity analysis with the FDTD method on structured grids," *IEEE Trans. Microwave Theory Tech.*, vol. 52, pp. 1207-1216, Apr. 2004.

[2] N. K. Nikolova, J. Zhu, D. Li, M. Bakr, and J. Bandler, "Sensitivities of network parameters with electromagnetic frequency domain simulators," *IEEE Trans. Microwave Theory Tech.* vol. 54, pp. 670-681, Feb. 2006.

[3] N. K. Nikolova, Ying Li, Yan Li, and M. H. Bakr, "Sensitivity analysis of scattering parameters with electromagnetic time-domain simulators," *IEEE Trans. Microwave Theory Tech.*, vol. 54, pp. 1589-1610, Apr. 2006.

[4] N. K. Nikolova, J. W. Bandler, and M. H. Bakr, "Adjoint techniques for sensitivity analysis in high-frequency structure CAD," *IEEE Trans. Microwave Theory Tech.*, vol. 52, pp. 403-419, Jan. 2004.

[5] J. Jin, *The Finite Element Method in Electromagnetics*, 2nd ed. New York: John Wiley & Sons, 2002.

[6] S. M. Ali, N. K. Nikolova, and M. H. Bakr, "Recent advances in sensitivity analysis with frequency-domain full-wave EM solvers," *Applied Computational Electromagnetics Society Journal.*, vol. 19, pp. 147-154, Nov. 2004

[7] E. J. Haug, K. K. Choi, and V. Komkov, *Design Sensitivity Analysis of Structural Systems.* Orlando, FL: Academic, 1986.

[8] M. D. Greenberg, *Advanced Engineering Mathematics*. Upper Saddle River, NJ: Prentice Hall, 1998, pp. 605.

[9] M. H. Bakr and N. K. Nikolova, "An adjoint variable method for time domain TLM with fixed structured grids," *IEEE Trans. Microwave Theory Tech.*, vol. 52, pp. 554-559, Feb. 2004.

[10] R. F. Harrington, *Time-Harmonic Electromagnetic Fields*. New York: McGraw-Hill book company, Inc., 1961.

[11] J. L. Volakis, A. Chatterjee, L. C. Kempel, *Finite Element Method for Electromagnetics*, New York: The Institute of Electrical and Electronics Engineers, Inc., 1998.

[12] H. Akel and J. P. Webb, "Design sensitivities for scattering-matrix calculation with tetrahedral edge elements," *IEEE Trans. Magnetics*, vol. 36, pp. 1043-1046, Jul. 2000.

Chapter 3

THE FINITE-DIFFERENCE FREQUENCY-DOMAIN SELF-ADJOINT SENSITIVITY ANALYSIS (FDFD-SASA)

3.1 Introduction

The self-adjoint sensitivity analysis (SASA) [1] is the most efficient method to compute the network parameter sensitivities with respect to designable parameters. No adjoint system analysis is needed. However, one prerequisite in the existing implementations of the SASA is the availability of the system matrix. This feature makes the SASA impractical or offsets its performance. This is because most commercial electromagnetic (EM) simulators do not provide access to the system matrix. Even if they do, the system matrix has to be exported to the computer disk. Since the system matrix is very large, reading/writing it from/to the disk is very time-consuming.

In this chapter, we propose a novel self-adjoint sensitivity analysis approach for *S*-parameters based on the finite-difference frequency-domain (FDFD) method, named finite-difference frequency-domain self-adjoint sensitivity analysis (FDFD-SASA) [2], [3]. The FDFD-SASA allows our sensitivity solver to be implemented as a software plug-in for volumetric partial-differential-equation-based commercial EM simulators. No system matrix is needed. The only requirement is that the EM simulator should be able to export the electric field at designated grid points. Compared to the system matrix, these electric-field files are negligibly small.

Sections 3.2 to 3.4 outline the theory of the FDFD-SASA and its independent central-node finite-difference grid. Sections 3.5 to 3.7 present the implementations of the FDFD-SASA for dielectric structures, as well as 3-D and infinitesimally thin metallic structures.

3.2 Adjoint Sensitivity Analysis Based on the FDFD Method

A frequency-domain EM problem in a linear medium can be described by the vector Helmholtz equation for the **E**-field

$$\nabla \times \mu_r^{-1} \nabla \times \mathbf{E} - \omega^2 \mu_0 \varepsilon_0 \varepsilon_r \mathbf{E} + j\omega\mu_0 \sigma \mathbf{E} = -j\omega\mu_0 \mathbf{J} \tag{3.1}$$

where ε_0, μ_0 are the permittivity and permeability of vacuum, while ε_r, μ_r, and σ are the medium relative permittivity, permeability, and conductivity,

respectively. In general, ε_r, μ_r, and σ are tensors. Here, for simplicity, we consider an isotropic medium where the material parameters are scalars. The current density **J** may represent impressed sources or induced secondary currents such as those induced in metals. The FDFD system equation can be produced after discretizing (3.1) using central finite differences:

$$\mathbb{C}^2\mathbf{E}+\alpha\cdot\mathbf{E}=\mathbf{G}. \tag{3.2}$$

In (3.2), the system coefficients are

$$\alpha=k_0^2\left(\varepsilon_r-j\frac{\sigma}{\omega\varepsilon_0}\right)\Delta h^2,\ \mathbf{G}=\beta\cdot\mathbf{J},\ \beta=j\omega\mu_0\Delta h^2 \tag{3.3}$$

where $k_0=\omega\sqrt{\mu_0\varepsilon_0}$, and $\Delta h=\min(\Delta x,\Delta y,\Delta z)$. The double-curl operator with a minus sign $\mathbb{C}^2$, i.e.,

$$\mathbb{C}^2\mathbf{E}\approx-\Delta h^2\cdot\nabla\times\mu_r^{-1}\nabla\times\mathbf{E}, \tag{3.4}$$

is derived using central finite differences [4], [5]. As an illustration, its x-component on a Yee-cell grid is [4]

$$\left(\mathbb{C}^2\mathbf{E}\right)_x=h_y^2D_{yy}^{\mu}E_x+h_z^2D_{zz}^{\mu}E_x-h_yh_xD_{yx}^{\mu}E_y-h_zh_xD_{zx}^{\mu}E_z \tag{3.5}$$

where

$$h_x=\frac{\Delta h}{\Delta x},\ h_y=\frac{\Delta h}{\Delta y},\ h_z=\frac{\Delta h}{\Delta z} \tag{3.6}$$

$$\begin{aligned}D_{yy}^{\mu}E_{x(x_0,y_0,z_0)}=&\frac{E_{x(x_0,y_0+\Delta y,z_0)}}{\mu_{r(x_0,y_0+\Delta y/2,z_0)}}+\frac{E_{x(x_0,y_0-\Delta y,z_0)}}{\mu_{r(x_0,y_0-\Delta y/2,z_0)}}-\\&\left[\frac{1}{\mu_{r(x_0,y_0+\Delta y/2,z_0)}}+\frac{1}{\mu_{r(x_0,y_0-\Delta y/2,z_0)}}\right]\cdot E_{x(x_0,y_0,z_0)}\end{aligned} \tag{3.7}$$

$$D_{yx}^{\mu}E_{y(x_0,y_0,z_0)} = \frac{E_{y(x_0+\Delta x/2,y_0+\Delta y/2,z_0)} - E_{y(x_0-\Delta x/2,y_0+\Delta y/2,z_0)}}{\mu_{r(x_0,y_0+\Delta y/2,z_0)}} - \frac{E_{y(x_0+\Delta x/2,y_0-\Delta y/2,z_0)} - E_{y(x_0-\Delta x/2,y_0-\Delta y/2,z_0)}}{\mu_{r(x_0,y_0-\Delta y/2,z_0)}}. \tag{3.8}$$

$D_{zz}^{\mu}E_x$ and $D_{zx}^{\mu}E_z$ can be derived similarly as (3.7) and (3.8), respectively. The y and z components of $\mathbb{C}^2\mathbf{E}$ can be obtained from $(\mathbb{C}^2\mathbf{E})_x$ in (3.5) using the cyclic substitution $x \rightarrow y \rightarrow z \rightarrow x$.

Note that the sensitivity analysis is independent from the field analysis engine and the method it utilizes. Thus, the sensitivity analysis may employ a sensitivity formula based on any valid system equations describing the EM problem. The field solution, which it uses and which is produced by the field analysis simulator, is unique according to the uniqueness theorem for the Helmholtz equation; therefore, the numerical method of obtaining this solution is unimportant, as long as it is accurate.

The frequency-domain generic EM response function can be defined as

$$F(\mathbf{E}, \boldsymbol{p}) = \iiint_{\Omega} f(\mathbf{E}, \boldsymbol{p}) d\Omega. \tag{3.9}$$

Here, Ω is the computational domain. The derivative with respect to p_n is

$$\frac{\partial F}{\partial p_n} = \frac{\partial^e F}{\partial p_n} + \iiint_{\Omega} \left(\frac{\partial f}{\partial E_x} \cdot \frac{\partial E_x}{p_n} + \frac{\partial f}{\partial E_y} \cdot \frac{\partial E_y}{p_n} + \frac{\partial f}{\partial E_z} \cdot \frac{\partial E_z}{p_n} \right) d\Omega. \tag{3.10}$$

Assume a perturbation Δp_n of the nth parameter. The respective FDFD system equation can be written as

$$\left(\mathbb{C}^2+\Delta_n\mathbb{C}^2\right)\cdot\left(\mathbf{E}+\Delta_n\mathbf{E}\right)+\left(\alpha+\Delta_n\alpha\right)\cdot\left(\mathbf{E}+\Delta_n\mathbf{E}\right)=\mathbf{G}+\Delta_n\mathbf{G}. \tag{3.11}$$

If we take (3.2) into account when expanding (3.11), we obtain

$$\mathbb{C}_n^2\Delta_n\mathbf{E}+\alpha_n\cdot\Delta_n\mathbf{E}+\Delta_n\mathbb{C}^2\mathbf{E}+\Delta_n\alpha\cdot\mathbf{E}-\Delta_n\mathbf{G}=0 \tag{3.12}$$

where

$$\mathbb{C}_n^2=\mathbb{C}^2+\Delta_n\mathbb{C}^2,\ \alpha_n=\alpha+\Delta_n\alpha. \tag{3.13}$$

Taking an inner product of (3.12) with a vector $\hat{\mathbf{E}}_n$, we have

$$\iiint_\Omega\left[\hat{\mathbf{E}}_n\cdot\left(\mathbb{C}_n^2\Delta_n\mathbf{E}+\alpha_n\cdot\Delta_n\mathbf{E}\right)+\hat{\mathbf{E}}_n\cdot\left(\Delta_n\mathbb{C}^2\mathbf{E}+\Delta_n\alpha\cdot\mathbf{E}-\Delta_n\mathbf{G}\right)\right]d\Omega=0. \tag{3.14}$$

Here, $\hat{\mathbf{E}}_n$ can be any arbitrary vector which exists in the computational domain Ω.

Let us consider one of the terms in (3.14):

$$I_c=\iiint_\Omega\left(\hat{\mathbf{E}}_n\cdot\mathbb{C}_n^2\Delta_n\mathbf{E}\right)d\Omega. \tag{3.15}$$

Here, $\mathbb{C}_n^2\Delta_n\mathbf{E}$ is an approximation of the double-curl operator taken at a point of the nth perturbed problem and applied to the difference field

$$\Delta_n\mathbf{E}=\mathbf{E}_n-\mathbf{E} \tag{3.16}$$

where $\mathbf{E}_n$ is the field solution of the nth perturbed problem and $\mathbf{E}$ is the one of the nominal problem. Applying (3.4) to (3.15), we have

$$I_c\approx\left(-\Delta h^2\right)\iiint_\Omega\hat{\mathbf{E}}_n\cdot\left(\nabla\times\mu_r^{-1}\nabla\times\Delta_n\mathbf{E}\right)d\Omega. \tag{3.17}$$

Using Green's theorem, (3.17) can be rewritten as

$$I_c \approx \left(-\Delta h^2\right) \iiint_{\Omega} \Delta_n \mathbf{E} \cdot \left(\nabla \times \mu_r^{-1} \nabla \times \hat{\mathbf{E}}_n\right) d\Omega$$
$$-\Delta h^2 \oiint_{S_\Omega} \left[\Delta_n \mathbf{E} \times \left(\mu_r^{-1} \nabla \times \hat{\mathbf{E}}_n\right) - \hat{\mathbf{E}}_n \times \left(\mu_r^{-1} \nabla \times \Delta_n \mathbf{E}\right)\right] \cdot d\boldsymbol{S}. \tag{3.18}$$

The general theory of the AVM shows that the adjoint EM problem is equivalent to the Maxwell equations where time runs backward, i.e., $\partial/\partial t$ is replaced by $-\partial/\partial\tau$ $(\tau = T - t)$ where T is the terminal time for the process. Hence, we have

$$\begin{cases} -\nabla \times \hat{\mathbf{H}}_n = j\omega\varepsilon \hat{\mathbf{E}}_n + \hat{\mathbf{J}}_n \\ \nabla \times \hat{\mathbf{E}}_n = j\omega\mu \hat{\mathbf{H}}_n. \end{cases} \tag{3.19}$$

The FDFD system equation for (3.19) is

$$\mathbb{C}^2 \hat{\mathbf{E}}_n + \alpha \cdot \hat{\mathbf{E}}_n = \hat{\mathbf{G}}_n. \tag{3.20}$$

Here, $\hat{\mathbf{G}}_n = \beta \cdot \hat{\mathbf{J}}_n$. The system coefficients in (3.20) are the same as in (3.2).

Using (3.19), (3.18) reduces as

$$I_c \approx \left(-\Delta h^2\right) \iiint_{\Omega} \Delta_n \mathbf{E} \cdot \left(\nabla \times \mu_r^{-1} \nabla \times \hat{\mathbf{E}}_n\right) d\Omega$$
$$-\Delta h^2 \oiint_{S_\Omega} \left(j\omega\mu\mu_r^{-1}\right) \left(\Delta_n \mathbf{E} \times \hat{\mathbf{H}}_n - \hat{\mathbf{E}}_n \times \Delta_n \mathbf{H}\right) \cdot d\boldsymbol{S} \tag{3.21}$$

where we have imposed a constraint on $\hat{\mathbf{E}}_n$ such that it satisfies (3.19). We refer to the quasi-electromagnetic field $\left(\hat{\mathbf{E}}_n, \hat{\mathbf{H}}_n\right)$ as the adjoint field. We also require that this adjoint field satisfies the same boundary conditions as the original system at the outer boundary S_Ω of the computational domain. At perfect electric

conductor (PEC) surfaces, the tangential components of both $\Delta_n\mathbf{E}$ and $\hat{\mathbf{E}}_n$ vanish; while at perfect magnetic conductor (PMC) surfaces, the tangential components of both $\hat{\mathbf{H}}_n$ and $\Delta_n\mathbf{H}$ vanish. Hence, the surface integral in (3.21) vanishes with either PEC or PMC boundary conditions. In the case of open or radiation problems, the boundary condition for $(\mathbf{E},\mathbf{H})$ is

$$\mathbf{H}=\frac{\boldsymbol{r}\times\mathbf{E}}{Z} \tag{3.22}$$

where $\boldsymbol{r}$ is the unit vector for the propagation direction, and Z is the intrinsic impedance of the medium. (3.19) and (3.22) show that $\left(\hat{\mathbf{E}}_n,\hat{\mathbf{H}}_n\right)$ has to satisfy such radiation boundary condition (RBC)

$$\hat{\mathbf{H}}_n=-\frac{\boldsymbol{r}\times\hat{\mathbf{E}}_n}{Z}. \tag{3.23}$$

Hence, in the far zone, we have

$$\Delta_n\mathbf{E}\times\hat{\mathbf{H}}_n-\hat{\mathbf{E}}_n\times\Delta_n\mathbf{H}=-\left(\mathbf{E}_n-\mathbf{E}\right)\times\frac{\boldsymbol{r}\times\hat{\mathbf{E}}_n}{Z}+\hat{\mathbf{E}}_n\times\frac{\boldsymbol{r}\times\left(\mathbf{E}_n-\mathbf{E}\right)}{Z}=0. \tag{3.24}$$

Therefore, the surface integral in (3.19) is zero for PEC, PMC, or RBC. Then, (3.21) can be simplified as

$$I_c\approx\left(-\Delta h^2\right)\iiint_{\Omega}\Delta_n\mathbf{E}\cdot\left(\nabla\times\mu_r^{-1}\nabla\times\hat{\mathbf{E}}_n\right)d\Omega=\iiint_{\Omega}\Delta_n\mathbf{E}\cdot\mathbb{C}_n^2\hat{\mathbf{E}}_n d\Omega. \tag{3.25}$$

From (3.15) and (3.25), we have

$$\iiint_{\Omega}\left(\hat{\mathbf{E}}_n\cdot\mathbb{C}_n^2\Delta_n\mathbf{E}\right)d\Omega=\iiint_{\Omega}\left(\Delta_n\mathbf{E}\cdot\mathbb{C}_n^2\hat{\mathbf{E}}_n\right)d\Omega. \tag{3.26}$$

Dividing (3.14) by Δp_n and taking (3.26) into account, we obtain

$$\iiint_{\Omega}\left[\left(\mathbb{C}_n^2\hat{\mathbf{E}}_n+\alpha_n\cdot\hat{\mathbf{E}}_n\right)\cdot\frac{\Delta_n\mathbf{E}}{\Delta p_n}+\hat{\mathbf{E}}_n\cdot\left(\frac{\Delta_n\mathbb{C}^2\mathbf{E}}{\Delta p_n}+\frac{\Delta_n\alpha}{\Delta p_n}\cdot\mathbf{E}-\frac{\Delta_n\mathbf{G}}{\Delta p_n}\right)\right]d\Omega=0\,.(3.27)$$

If we set

$$\mathbb{C}_n^2\hat{\mathbf{E}}_n+\alpha_n\cdot\hat{\mathbf{E}}_n=\frac{\partial f}{\partial E_x}\hat{\mathbf{x}}+\frac{\partial f}{\partial E_y}\hat{\mathbf{y}}+\frac{\partial f}{\partial E_z}\hat{\mathbf{z}} \tag{3.28}$$

and approximate $\Delta_n\mathbf{E}/\Delta p_n$ by $\partial\mathbf{E}/\partial p_n$, (3.27) can be derived as

$$\iiint_{\Omega}\left(\frac{\partial f}{\partial E_x}\cdot\frac{\partial E_x}{p_n}+\frac{\partial f}{\partial E_y}\cdot\frac{\partial E_y}{p_n}+\frac{\partial f}{\partial E_z}\cdot\frac{\partial E_z}{p_n}+\hat{\mathbf{E}}_n\cdot\frac{\Delta_n R(\mathbf{E})}{\Delta p_n}\right)d\Omega\approx 0 \tag{3.29}$$

where

$$\frac{\Delta_n R(\mathbf{E})}{\Delta p_n}=\frac{\Delta_n\mathbb{C}^2\mathbf{E}}{\Delta p_n}+\frac{\Delta_n\alpha}{\Delta p_n}\cdot\mathbf{E}-\frac{\Delta_n\mathbf{G}}{\Delta p_n}. \tag{3.30}$$

Comparing (3.29) with (3.10), the adjoint sensitivity formula based on the FDFD method can be written as

$$\frac{\partial F}{\partial p_n}\approx\frac{\partial^e F}{\partial p_n}-\iiint_{\Omega}\hat{\mathbf{E}}_n\cdot\frac{\Delta R(\mathbf{E})}{\Delta p_n}d\Omega\,. \tag{3.31}$$

Note that the adjoint field $\hat{\mathbf{E}}_n$ is uniquely defined by the discretized vector Helmholtz equation (3.28) and the boundary conditions at S_Ω which are the same as in the original system. In (3.28), the subscript n emphasizes that all material parameters in the computational domain must represent the structure which is perturbed in the nth parameter. That is why the solution to (3.28) is denoted as $\hat{\mathbf{E}}_n$.

Equation (3.31) gives the second-order sensitivity formula, which takes into account the second-order perturbation terms $\Delta_n\mathbb{C}^2\mathbf{E}\cdot\Delta_n\mathbf{E}$ and $\Delta_n\alpha\cdot\Delta_n\mathbf{E}$ [see (3.11) and (3.12)]. If the changes in the system coefficients ($\Delta_n\mathbb{C}^2$ and $\Delta_n\alpha$) as well as the change in the field solution $\Delta_n\mathbf{E}$ are small enough so that the second-order terms can be neglected, the finite-difference operators $\Delta_n\mathbb{C}^2/\Delta p_n$ and $\Delta_n\alpha/\Delta p_n$ can be accurately represented by the analytical derivative operators $\partial\mathbb{C}^2/\partial p_n$ and $\partial\alpha/\partial p_n$, provided the latter exist.

It is straightforward to repeat the analysis above for the case when (3.12) contains first-order terms only. The result is the well-known exact sensitivity formula

$$\frac{\partial F}{\partial p_n}=\frac{\partial^e F}{\partial p_n}-\iiint_\Omega\hat{\mathbf{E}}\cdot\frac{\partial R(\mathbf{E})}{\partial p_n}d\Omega \tag{3.32}$$

where

$$\frac{\partial R(\mathbf{E})}{\partial p_n}=\frac{\partial\mathbb{C}^2\mathbf{E}}{\partial p_n}+\frac{\partial\alpha}{\partial p_n}\cdot\mathbf{E}-\frac{\partial\mathbf{G}}{\partial p_n}. \tag{3.33}$$

Note that (3.33) requires the analytical derivatives of the system coefficients. In contrast, (3.30) operates on finite-difference ratios of the system coefficients. Another consequence of neglecting the second-order perturbation terms is that now the adjoint field $\hat{\mathbf{E}}$ must satisfy the discretized vector Helmholtz equation for the nominal structure

$$\mathbb{C}^2\hat{\mathbf{E}}+\alpha\cdot\hat{\mathbf{E}}=\frac{\partial f}{\partial E_x}\hat{\mathbf{x}}+\frac{\partial f}{\partial E_y}\hat{\mathbf{y}}+\frac{\partial f}{\partial E_z}\hat{\mathbf{z}}. \tag{3.34}$$

Thus, $\hat{\mathbf{E}}$ is parameter-independent. As before, the adjoint solution of (3.34) must fulfill the same boundary conditions as the original solution $\mathbf{E}$.

The exact sensitivity theory [see formulas (3.32)-(3.34)] is applicable with numerical systems whose coefficients are analytical functions of the optimizable parameters. For example, the FDFD method allows for exact sensitivity calculations with respect to material parameters since α and the components of $\mathbb{C}^2$ are analytical functions of $(\varepsilon_r,\ \sigma)$ and μ_r, respectively.

However, the exact theory is not applicable with shape parameters on a finite-difference grid because the shape parameters belong to a discrete space. They are constrained to values that are integer multiples of the grid step size. Thus, the system coefficients are not analytical functions of the shape parameters. In the case of shape parameters, the second-order formula (3.31) must be used. However, there, the adjoint field $\hat{\mathbf{E}}_n$ is formally dependent on the parameter perturbation Δp_n, i.e., for each shape parameter there is a different adjoint field. These adjoint fields, however, can all be derived from the adjoint field of the nominal (unperturbed) structure by a simple one-to-one mapping, which will be discussed in more detail in the following sections. Thus, in both cases, the exact formula and the discrete second-order formula, only one adjoint analysis is necessary to calculate the adjoint field.

3.3 The FDFD-SASA for *S*-parameters [2], [3]

In this work, we focus on the *S*-parameter sensitivity analysis based on the volume **E**-field solution in the frequency domain such as those produced by the finite-element method (FEM). To obtain the full scattering matrix of a *K*-port structure for a mode υ, *K* simulations are carried out with one of the ports being excited while the rest of the ports are matched. If the *j*th port is excited, the S_{kj} parameters can be defined as [1]

$$S_{kj}^{(\upsilon)} = \sqrt{\frac{Z_j^{(\upsilon)}}{Z_k^{(\upsilon)}}}\left[\frac{\iint_{k-\text{port}} \left(\mathbf{a}_n \times \mathbf{E}_j\right)\cdot\left(\mathbf{a}_n \times \mathbf{e}_k^{(\upsilon)}\right) dS_k}{\iint_{j-\text{port}} \left(\mathbf{a}_n \times \mathbf{E}_j^{\text{inc}}\right)\cdot\left(\mathbf{a}_n \times \mathbf{e}_j^{(\upsilon)}\right) dS_j} - \delta_{kj}\right], \quad \delta_{kj} = \begin{cases} 1, & k = j \\ 0, & k \neq j \end{cases}. \tag{3.35}$$

Here, $\mathbf{a}_n$ is the unit normal to the respective port surface, $Z_\zeta^{(\upsilon)}$ $(\zeta = k, j)$ is the wave impedance of the ζth port, and $\mathbf{e}_\zeta^{(\upsilon)}$ is the modal vector of the ζth port, which gives the normalized distribution of the field across the port. $\mathbf{E}_j^{\text{inc}}$ is the incident field at the *j*th port, and $\mathbf{E}_j$ is the **E**-field solution resulting from the excitation at the *j*th port. The modal vectors $\mathbf{e}_\zeta^{(\upsilon)}$ form an orthonormal basis

$$\iint_{\zeta-\text{port}} \left(\mathbf{e}_\zeta^{(\upsilon)} \cdot \mathbf{e}_\zeta^{(\upsilon')}\right) dS_\zeta = \delta_{\upsilon\upsilon'} \tag{3.36}$$

where $\delta_{\upsilon\upsilon'} = 1$ if the modes υ and υ' are the same , and $\delta_{\upsilon\upsilon'} = 0$ otherwise.

$\mathbf{E}_j^{\text{inc}}$ can be expressed as a superposition of all modes

$$\mathbf{E}_j^{\text{inc}} = \sum_{\upsilon} E_{0j}^{(\upsilon)} \mathbf{e}_\zeta^{(\upsilon)} \tag{3.37}$$

where $E_{0j}^{(\upsilon)}$ is the magnitude of the incident field of the υ mode. Taking (3.36) and (3.37) into account, (3.35) reduces as

$$S_{kj}^{(\upsilon)} = \sqrt{\frac{Z_j^{(\upsilon)}}{Z_k^{(\upsilon)}}} \left[\frac{\iint_{k-\text{port}} \left(\mathbf{a}_n \times \mathbf{E}_j^{(\upsilon)}\right) \cdot \left(\mathbf{a}_n \times \mathbf{e}_k^{(\upsilon)}\right) dS_k}{E_{0j}^{(\upsilon)}} - \delta_{kj} \right]. \tag{3.38}$$

Since we consider the S-parameter sensitivities of a single mode, the superscript υ is omitted from now on. If the designable parameter p_n does not relate to the ports, $\partial^e S_{kj}/\partial p_n$ is zero. Hence, from (3.38), we obtain

$$\frac{\partial S_{kj}}{\partial p_n} = \sqrt{\frac{Z_j}{Z_k}} \cdot \frac{1}{E_{0j}} \cdot \iint_{k-\text{port}} \frac{\partial \mathbf{E}_j}{\partial p_n} \cdot \mathbf{e}_k dS_k \,. \tag{3.39}$$

In section 3.2, we have proved that the surface integral in (3.18) vanishes at S_Ω where PEC, PMC or RBC is imposed. Here, let us consider portions of S_Ω that correspond to the ports where the surface integral does not necessarily vanish. (3.18) can be rewritten as

$$\begin{aligned} I_c \approx & \left(-\Delta h^2\right) \iiint_\Omega \Delta_n \mathbf{E} \cdot \left(\nabla \times \mu_r^{-1} \nabla \times \hat{\mathbf{E}}_n\right) d\Omega \\ & - \Delta h^2 \sum_{\zeta=1}^{K} \iint_{S_\zeta} \mu_r^{-1} \left[\Delta_n \mathbf{E} \times \left(\nabla \times \hat{\mathbf{E}}_n\right) - \hat{\mathbf{E}}_n \times \left(\nabla \times \Delta_n \mathbf{E}\right) \right] \cdot d\boldsymbol{S}_\zeta \\ = & \iiint_\Omega \Delta_n \mathbf{E} \cdot \mathbb{C}_n^2 \hat{\mathbf{E}}_n d\Omega \\ & - \Delta h^2 \sum_{\zeta=1}^{K} \iint_{S_\zeta} \mu_r^{-1} \left[\Delta_n \mathbf{E} \times \left(\nabla \times \hat{\mathbf{E}}_n\right) - \hat{\mathbf{E}}_n \times \left(\nabla \times \Delta_n \mathbf{E}\right) \right] \cdot d\boldsymbol{S}_\zeta . \end{aligned} \tag{3.40}$$

Substituting (3.40) into (3.14), we have

$$\begin{aligned}&\iiint_{\Omega}\Delta_n\mathbf{E}\cdot\left(\mathbb{C}_n^2\hat{\mathbf{E}}_n+\alpha_n\cdot\hat{\mathbf{E}}_n\right)d\Omega+\iiint_{\Omega}\hat{\mathbf{E}}_n\cdot\left(\Delta_n\mathbb{C}^2\mathbf{E}+\Delta_n\alpha\cdot\mathbf{E}-\Delta_n\mathbf{G}\right)d\Omega\\&=\Delta h^2\sum_{\zeta=1}^{K}\iint_{S_\zeta}\mu_r^{-1}\left[\Delta_n\mathbf{E}\times\left(\nabla\times\hat{\mathbf{E}}_n\right)-\hat{\mathbf{E}}_n\times\left(\nabla\times\Delta_n\mathbf{E}\right)\right]\cdot d\boldsymbol{S}_\zeta.\end{aligned}\tag{3.41}$$

Dividing (3.41) by Δp_n and approximating $\Delta_n\mathbf{E}/\Delta p_n$ by $\partial\mathbf{E}/\partial p_n$, we obtain

$$\begin{aligned}&\iiint_{\Omega}\frac{\partial\mathbf{E}}{\partial p_n}\cdot\left(\mathbb{C}_n^2\hat{\mathbf{E}}_n+\alpha_n\cdot\hat{\mathbf{E}}_n\right)d\Omega+\iiint_{\Omega}\hat{\mathbf{E}}_n\cdot\left(\frac{\Delta_n\mathbb{C}^2\mathbf{E}}{\Delta p_n}+\frac{\Delta_n\alpha}{\Delta p_n}\cdot\mathbf{E}-\frac{\Delta_n\mathbf{G}}{\Delta p_n}\right)d\Omega\\&\approx\Delta h^2\sum_{\zeta=1}^{K}\iint_{S_\zeta}\mu_r^{-1}\left[\frac{\partial\mathbf{E}}{\partial p_n}\times\left(\nabla\times\hat{\mathbf{E}}_n\right)-\hat{\mathbf{E}}_n\times\left(\nabla\times\frac{\partial\mathbf{E}}{\partial p_n}\right)\right]\cdot d\boldsymbol{S}_\zeta.\end{aligned}\tag{3.42}$$

Here we consider S-parameter sensitivity calculations, whose local response $f(\mathbf{E},\boldsymbol{p})$ does not depend on the field solution in Ω but rather at S_Ω. Hence, the adjoint solution satisfies

$$\mathbb{C}_n^2\hat{\mathbf{E}}_n+\alpha_n\cdot\hat{\mathbf{E}}_n=\hat{\mathbf{G}}_n=0.\tag{3.43}$$

Note that in the case of a source-free but boundary-excited problem, the original solution also satisfies the homogeneous equation

$$\mathbb{C}^2\mathbf{E}+\alpha\cdot\mathbf{E}=0.\tag{3.44}$$

FEM simulators carry out the excitation at the ζth port through the boundary condition

$$\boldsymbol{n}\times\left(\nabla\times\mathbf{E}_\zeta\right)+\gamma_\zeta\boldsymbol{n}\times\left(\boldsymbol{n}\times\mathbf{E}_\zeta\right)=\mathbf{U}_\zeta^{\text{inc}}\tag{3.45}$$

where

$$\mathbf{U}_\zeta^{\text{inc}}=-2\gamma_\zeta\mathbf{E}_\zeta^{\text{inc}}=-2\gamma_\zeta E_{0\zeta}\mathbf{e}_\zeta\tag{3.46}$$

and $\boldsymbol{n}$ is the outward normal at the port cross-section [1]. The rest of the ports are matched with the boundary condition

$$\boldsymbol{n}\times\left(\nabla\times\mathbf{E}_\zeta\right)+\gamma_\zeta\boldsymbol{n}\times\left(\boldsymbol{n}\times\mathbf{E}_\zeta\right)=0\,. \tag{3.47}$$

In a source-free problem excited through the boundary conditions, (3.42) reduces as

$$\begin{aligned}&\iiint_\Omega \hat{\mathbf{E}}_n\cdot\frac{\Delta_n R(\mathbf{E})}{\Delta p_n}d\Omega\\ &\approx \Delta h^2\sum_{\zeta=1}^{K}\iint_{S_\zeta}\mu_r^{-1}\left[\frac{\partial\mathbf{E}}{\partial p_n}\times\left(\nabla\times\hat{\mathbf{E}}_n\right)-\hat{\mathbf{E}}_n\times\left(\nabla\times\frac{\partial\mathbf{E}}{\partial p_n}\right)\right]\cdot d\boldsymbol{S}_\zeta\,.\end{aligned} \tag{3.48}$$

Applying the port boundary condition (3.45) to the surface integral in (3.48), we have

$$\begin{aligned}S_\Sigma&=\sum_{\zeta=1}^{K}\iint_{S_\zeta}\mu_r^{-1}\left[\frac{\partial\mathbf{E}}{\partial p_n}\times\left(\nabla\times\hat{\mathbf{E}}_n\right)-\hat{\mathbf{E}}_n\times\left(\nabla\times\frac{\partial\mathbf{E}}{\partial p_n}\right)\right]\cdot d\boldsymbol{S}_\zeta\\ &=\sum_{\zeta=1}^{K}\iint_{S_\zeta}\mu_r^{-1}\left[\frac{\partial\mathbf{E}}{\partial p_n}\cdot\left(\nabla\times\hat{\mathbf{E}}_n\right)\times\boldsymbol{n}-\hat{\mathbf{E}}_n\cdot\left(\nabla\times\frac{\partial\mathbf{E}}{\partial p_n}\right)\times\boldsymbol{n}\right]\cdot dS_\zeta\\ &=\sum_{\zeta=1}^{K}\iint_{S_\zeta}\mu_r^{-1}\left[\frac{\partial\mathbf{E}}{\partial p_n}\cdot\left(\gamma_\zeta\boldsymbol{n}\times\boldsymbol{n}\times\hat{\mathbf{E}}_n-\hat{\mathbf{U}}_\zeta^{\text{inc}}\right)-\hat{\mathbf{E}}_n\cdot\left(\gamma_\zeta\boldsymbol{n}\times\boldsymbol{n}\times\frac{\partial\mathbf{E}}{\partial p_n}-\frac{\partial\hat{\mathbf{U}}_\zeta^{\text{inc}}}{\partial p_n}\right)\right]\cdot dS_\zeta\\ &=\sum_{\zeta=1}^{K}\iint_{S_\zeta}\mu_r^{-1}\left\{\frac{\partial\mathbf{E}}{\partial p_n}\cdot\left[-\gamma_\zeta\left(\hat{\mathbf{E}}_n\right)_t-\hat{\mathbf{U}}_\zeta^{\text{inc}}\right]-\hat{\mathbf{E}}_n\cdot\left(-\gamma_\zeta\frac{\partial\mathbf{E}_t}{\partial p_n}\right)\right\}\cdot dS_\zeta\\ &=\sum_{\zeta=1}^{K}\iint_{S_\zeta}\mu_r^{-1}\left(-\frac{\partial\mathbf{E}}{\partial p_n}\cdot\hat{\mathbf{U}}_\zeta^{\text{inc}}\right)\cdot dS_\zeta\,.\end{aligned} \tag{3.49}$$

We set the adjoint excitation $\hat{\mathbf{U}}_\zeta^{\text{inc}}$ as

$$\hat{\mathbf{U}}_{\zeta}^{\text{inc}} = \begin{cases} 0, & \zeta \neq k \\ -\sqrt{\dfrac{Z_j}{Z_k}} \cdot \dfrac{1}{E_{0j}} \mathbf{e}_k, & \zeta = k \end{cases} \tag{3.50}$$

and assume that $\mu_r = 1$ at the kth port, which is a simpler and often encountered scenario. Taking (3.39) and (3.48)-(3.50) into account, we obtain

$$\frac{\partial S_{kj}}{\partial p_n} = S_{\Sigma} \approx \frac{1}{\Delta h^2} \iiint_{\Omega} \left(\hat{\mathbf{E}}_{kj}\right)_n \cdot \frac{\Delta_n R(\mathbf{E}_j)}{\Delta p_n} d\Omega . \tag{3.51}$$

Note that adjoint solution $\left(\hat{\mathbf{E}}_{kj}\right)_n$ corresponds to the adjoint problem where all other ports are matched when the kth port is excited with (3.50). A linear relationship between $\hat{\mathbf{U}}_k^{\text{inc}}$ and $\mathbf{U}_k^{\text{inc}}$ exists, i.e.,

$$\hat{\mathbf{U}}_k^{\text{inc}} = \sqrt{\frac{Z_j}{Z_k}} \cdot \frac{1}{2\gamma_k E_{0j} E_{0k}} \cdot \mathbf{U}_k^{\text{inc}} . \tag{3.52}$$

Considering (3.2) and (3.20), (3.52) implies the same relationship between $\hat{\mathbf{E}}_{kj}$ and $\mathbf{E}_k$, i.e.,

$$\hat{\mathbf{E}}_{kj} = \kappa_{kj} \cdot \mathbf{E}_k = \sqrt{\frac{Z_j}{Z_k}} \cdot \frac{1}{2\gamma_k E_{0j} E_{0k}} \cdot \mathbf{E}_k . \tag{3.53}$$

Here, κ_{kj} is called the self-adjoint constant, which is

$$\kappa_{kj} = \sqrt{\frac{Z_j}{Z_k}} \cdot \frac{1}{2\gamma_k E_{0k} E_{0j}} . \tag{3.54}$$

$E_{0\zeta}$ $(\zeta = k, j)$ is obtained from the incident field solution at the ports directly using

$$E_{0\zeta} = \sqrt{\iint\limits_{\zeta-\text{port}} \mathbf{E}_{\zeta}^{\text{inc}} \cdot \mathbf{E}_{\zeta}^{\text{inc}} d\boldsymbol{s}_{\zeta}} \,. \tag{3.55}$$

An FEM analysis provides the total field solution at the ports, not the incident field solution. The port analysis in Ansoft HFSS does not allow the users to access the incident field solution at the ports. In order to obtain $E_{0\zeta}$, a homogeneous waveguide with a cross-section identical to that of the ζth port is simulated. This waveguide should be long enough so that no spurious solution affects the ports. The field solution at the ports is considered the same as the incident field.

The sensitivity formula for *S*-parameters based on the FDFD-SASA with respect to the shape parameters is obtained as

$$\frac{\partial S_{kj}}{\partial p_n} \approx \frac{\kappa_{kj}}{\Delta h^2} \cdot \iiint\limits_{\Omega} (\mathbf{E}_k)_n \cdot \frac{\Delta_n R(\mathbf{E}_j)}{\Delta p_n} d\Omega \quad n = 1, 2, \ldots, N \tag{3.56}$$

where

$$\frac{\Delta_n R(\mathbf{E}_j)}{\Delta p_n} = \frac{\Delta_n \mathbb{C}^2 \mathbf{E}_j}{\Delta p_n} + \frac{\Delta_n \alpha}{\Delta p_n} \cdot \mathbf{E}_j - \frac{\Delta_n \mathbf{G}_j}{\Delta p_n} \,. \tag{3.57}$$

Here, $\mathbf{G}_j = \beta \cdot \mathbf{J}_j^{\text{ind}}$ arises from the induced currents at metallic objects [5], which are functions of the field solution, $\mathbf{J}_j^{\text{ind}}(\mathbf{E}_j)$. The shape parameters can assume only discrete values snapped to the finite-difference grid of the sensitivity solver, i.e., $\Delta p_n = \pm\Delta x$, or $\pm\Delta y$, or $\pm\Delta z$ [4], [5]. Thus, the system coefficients are not differentiable. The grid of the sensitivity solver is independent of that of the

simulator. The grid step sizes Δx, Δy, and Δz are usually chosen to be equal to one respective FEM-edge length. $\mathbf{E}_\zeta$ $(\zeta = k, j)$ in (3.56) denotes the field solution resulting from the simulation when port ζ is excited. $(\mathbf{E}_k)_n$ is obtained from $\mathbf{E}_k$ with a simple field-mapping procedure [4], [8]. More details are shown in the following sections.

The FDFD-SASA for *S*-parameters with respect to material parameters is exact in the sense that the system coefficient derivatives are analytical with respect to the material parameters. The sensitivity formula is

$$\frac{\partial S_{kj}}{\partial p_n} = \frac{\kappa_{kj}}{\Delta h^2} \cdot \iiint_{\Omega} \mathbf{E}_k \cdot \frac{\partial R(\mathbf{E}_j)}{\partial p_n} d\Omega \quad n = 1, 2, \ldots, N \tag{3.58}$$

where

$$\frac{\partial R(\mathbf{E}_j)}{\partial p_n} = \frac{\partial \mathbb{C}^2 \mathbf{E}_j}{\partial p_n} + \frac{\partial \alpha}{\partial p_n} \cdot \mathbf{E}_j . \tag{3.59}$$

The first term in (3.59) is an analytical function of the material parameter μ_r, while the second one is a function of ε_r and σ, e.g., $\partial\alpha/\partial\varepsilon_r = k_0^2 \Delta h^2$, $\partial\alpha/\partial\sigma = -jk_0^2 \Delta h^2 / \omega\varepsilon_0$. The other difference with (3.57) is the field solution $\mathbf{E}_k$, which corresponds to the nominal structure, not the perturbed one. Field mapping is not needed.

For 2-D problems where only the vertical **E** component contributes to the sensitivity computation, (3.56) reduces as

$$\frac{\partial S_{kj}}{\partial p_n} \approx \frac{\kappa_{kj} b}{\Delta h^2} \cdot \iint_S (E_{zk})_n \cdot \frac{\Delta_n R(E_{zj})}{\Delta p_n} dS \quad n = 1,2,\ldots,N \tag{3.60}$$

where

$$\frac{\Delta_n R(E_{zj})}{\Delta p_n} = \frac{\Delta_n \mathbb{C}^2 E_{zj}}{\Delta p_n} + \frac{\Delta_n \alpha}{\Delta p_n} \cdot E_{zj} - \frac{\Delta_n \mathrm{G}_{zj}}{\Delta p_n}. \tag{3.61}$$

Here, E_z is the vertical component, and b is the vertical height of the original 3-D structure. (3.58) and (3.59) can be simplified similarly.

With (3.56) and (3.58), our sensitivity solver becomes independent from the simulator's grid, system equations and discretization method. It uses its own FD grid and FDFD system equations. The only requirement of the simulator is to export the field solution at the perturbation grid points, and at the corresponding excitation ports (to compute the self-adjoint constant). The perturbation region is the region where the system coefficients change due to the perturbation of the designable parameters. Hence, the time to export and read the exported field-solution files is negligible compared to the time necessary to export the system matrix, which was necessary in the previous implementation of the SASA. Also, our algorithm performs *S*-parameter sensitivity analysis through a self-adjoint formulation which eliminates the need to perform adjoint system analysis and greatly simplifies the implementation. Its computational overhead is a fraction of that of the simulation itself.

Up to now, the sensitivity formula is obtained under the assumption that $\mu_r = 1$ at the *k*th port when considering the derivatives of the S_{kj} parameter. It is

straightforward to derive the sensitivity formula for the general case of a magnetic port where μ_r does not have to be homogeneous. For example, in that case, the sensitivity formula (3.56) becomes

$$\frac{\partial S_{kj}}{\partial p_n} \approx \frac{\kappa_{kj}}{\Delta h^2} \cdot \iiint_{\Omega} \mu_r \left(\mathbf{E}_k\right)_n \cdot \frac{\Delta_n R(\mathbf{E}_j)}{\Delta p_n} d\Omega \quad n = 1, 2, \ldots, N. \tag{3.62}$$

3.4 Central-node Finite-difference Grid [3]

Figure 3.1 illustrates the FD grid used by the sensitivity solver superimposed on the FEM mesh of the simulator. Figure 3.1a shows a 2-D *H*-plane cut of the grid at the location of one of the dielectric rectangular posts in a dielectric-resonator filter. The shaded area shows the location of the dielectric post. The crosses indicate locations where the vertical **E** component is recorded on a Yee-cell grid in order to compute the *S*-parameter derivatives with respect to the shape parameter p_n. The dots indicate these locations on a central-node grid. Figure 3.1b shows a similar cut at the location of a metallic septum in an *H*-plane filter.

Until now, our sensitivity solvers have used a FD grid based on the Yee cell [5], [9], which is common in FDTD algorithms. Its advantage is that the **E**-field boundary conditions at metallic objects are satisfied exactly. Its disadvantage is the complicated implementation in 3-D problems where the field components are computed on different (staggered) grids.

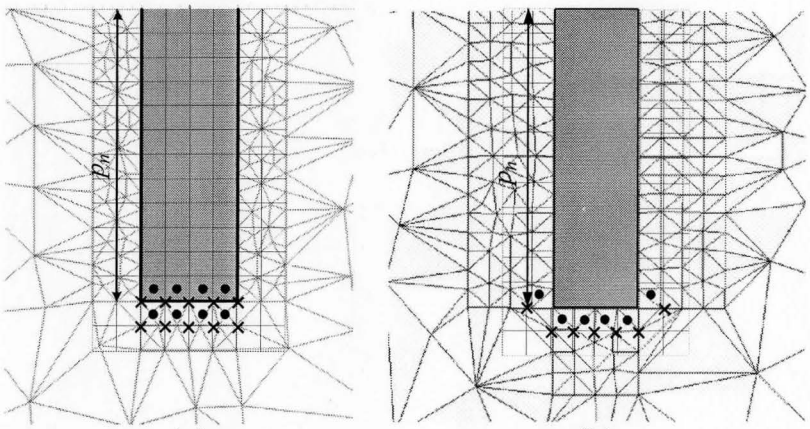

Figure 3.1 A 2-D cut of the discretization grid used by the finite-element simulator (Ansoft HFSS) superimposed with the finite-difference grid used by the sensitivity solver: (a) dielectric post; (b) metallic septum. The vertical field component is recorded at grid points indicated by: (i) crosses—for the original Yee-cell grid; (ii) dots—for the proposed central-node grid.

Furthermore, we have found that sensitivity calculations with time-domain field solutions are more accurate if a central-node cell is used instead of the Yee cell in the case of dielectric objects, especially when the structures involve high-contrast dielectric interfaces [10]. There are two reasons for this: (1) the value of the permittivity at a dielectric interface, which is needed in the sensitivity formula, is ambiguous (weighted averaging is usually used in the FDTD methods); and (2) the local field solution is the least accurate at points lying directly on the interface. The central-node FD cell is characterized by a single node where all three **E**-field components are calculated. This feature significantly simplifies the implementation especially for 3-D metallic structures.

However, the question remains whether this grid is appropriate for the calculation of sensitivities with respect to the shape parameters of metallic objects since now tangential **E** components are taken half a step away from metallic walls. The work in [3] demonstrates that the central-node grid is suitable for sensitivity analysis of metallic objects—there is no loss of accuracy compared to the Yee-cell grid.

3.5 Implementation of the FDFD-SASA for Dielectric Structures

3.5.1 The FDFD-SASA algorithm

No induced current exists in dielectric structures. Besides, field solution does not vanish with the perturbation, which results in no change of the coefficients of the double-curl in (3.57). Hence, the system residual derivatives can be simplified as

$$\frac{\Delta_n R(\mathbf{E}_j)}{\Delta p_n} = \frac{\Delta_n \alpha}{\Delta p_n} \cdot \mathbf{E}_j \tag{3.63}$$

$$\frac{\partial R(\mathbf{E}_j)}{\partial p_n} = \frac{\partial \alpha}{\partial p_n} \cdot \mathbf{E}_j \tag{3.64}$$

where (3.63) applies to shape parameters while (3.64) applies to material parameters. The implementation for 3-D problems is the same as in 2-D problems.

The proposed *S*-parameter sensitivity algorithm can be performed with the following steps.

Step 1: Compute the self-adjoint constant. Simulate a long enough homogeneous waveguide whose ports are identical to the ζth port $(\zeta = k, j)$. Export the field solution at one of the ports of the ζth waveguide. Compute κ_{kj} with (3.54) and (3.55).

Step 2: Simulate the nominal problem. Record field solutions $\mathbf{E}_j$ and $\mathbf{E}_k$ at the perturbation grid points.

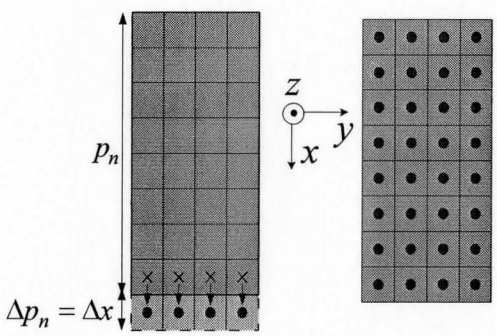

Figure 3.2 Perturbation grid points for the computation of *S*-parameter derivatives with respect to designable parameters of a dielectric post: (a) shape parameter p_n; (b) material parameter p_n. The dark shaded area in (a) represents the nominal shape of the post while the light shaded area is an assumed perturbation area corresponding to a perturbation $\Delta p_n = \Delta x$.

If the shape parameter p_n of a dielectric post is perturbed as $p_n + \Delta p_n$ shown in figure 3.2a, the system coefficient α in the light gray region changes. $\mathbf{E}_j$ is recorded at the dots in figure 3.2a. $(\mathbf{E}_k)_n$ is also need at the dots in figure 3.2a. However, $(\mathbf{E}_k)_n$ must represent the solution of the *n*th perturbed problem (post length is $p_n + \Delta p_n$). According to perturbation theory, we can estimate $(\mathbf{E}_k)_n$ at the dots in the perturbed problem by assuming that it is the same as the field in the nominal problem at the crosses, i.e., $(\mathbf{E}_k)_n^{i,j,k} = \mathbf{E}_k^{i-1,j,k}$. In summary, we need to export $\mathbf{E}_j$ at the dots and $\mathbf{E}_k$ at the crosses. Then, we assign $\mathbf{E}_k$ at the crosses to $(\mathbf{E}_k)_n$ at the dots.

If the material parameters of this dielectric post change, the system coefficient α changes in the whole post. As a result, $\mathbf{E}_j$ and $\mathbf{E}_k$ are needed at the dots in figure 3.2b.

Step 3: Compute the system residual derivatives with (3.63) and (3.64).

Step 4: Compute S_{kj} derivative with the discretized form of the FDFD-SASA formula. For example, the discretized form of (3.56) can be written as

$$\frac{\partial S_{kj}}{\partial p_n} \approx \frac{\kappa_{kj}}{\Delta h^2} \cdot \sum_{\Omega} \left[(\mathbf{E}_k)_n \cdot \frac{\Delta_n R(\mathbf{E}_j)}{\Delta p_n} \cdot \Delta x \Delta y \Delta z \right]_{\Omega}. \tag{3.65}$$

3.5.2 2-D example: *H*-plane dielectric-resonator filter [2]

We first validate our technique with an *H*-plane dielectric-resonator filter [11], built from three identical rectangular ceramic posts. Its *H*-plane (determined by the propagation vector and $\boldsymbol{H}$ vector) view is shown in figure 3.3. The waveguide cross-section is $a \times b = 3.48 \times 1.6\ \text{cm}^2$.

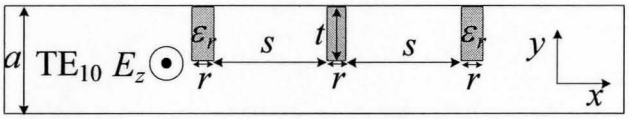

Figure 3.3 *H*-plane view of the dielectric-resonator filter.

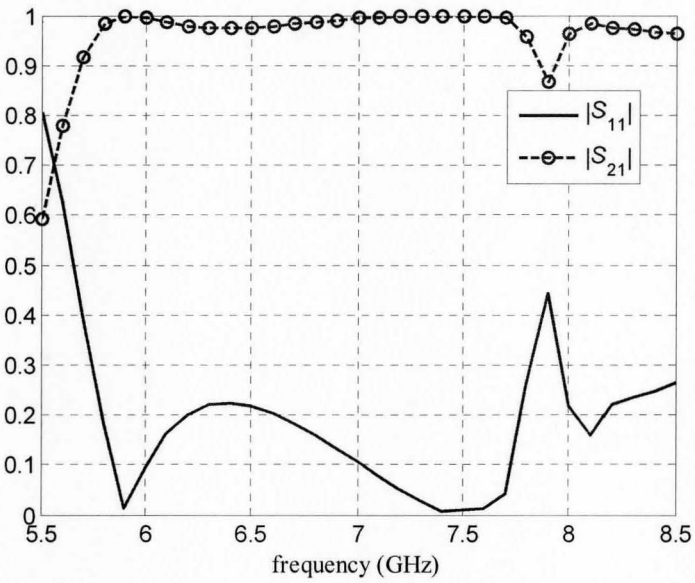

Figure 3.4 $|S_{11}|$ and $|S_{21}|$ of the structure shown in figure 3.3.

The simulation is performed at $f_0 = 6.88$ GHz. Therefore, only the dominant TE_{10} mode is analyzed. Here, the designable parameters are: the relative permittivity of the posts ε_r, the length of the posts t, the width of the posts r, and the distance between the posts s. The nominal design is $\varepsilon_r = 38.5$, $t = 0.2a$, $r = 0.06a$, and $s = 0.32\lambda$, where λ is the wavelength of the TE_{10} mode at f_0. Figure 3.4 shows $|S_{11}|$ and $|S_{21}|$ at the nominal state.

In all figures, the derivative curves obtained via central finite differences at the response level (obtained from the responses at the state of $p_n + \Delta p_n$ and $p_n - \Delta p_n$) are marked with CFD. Since the filter cannot be analyzed analytically, these curves serve as a reference even though not a reliable one. The curves obtained with our FDFD-SASA technique are marked with FDFD-SASA.

Figures 3.5 and 3.6 show the derivative curves of $|S_{11}|$ and $|S_{21}|$ with respect to ε_r, respectively. The derivatives of their respective angles are plotted in figures 3.7 and 3.8. Figures 3.9 to 3.20 show the corresponding derivative curves for the shape parameters t, r, and s.

In order to obtain the CFD derivative curves for ε_r, a step of $\Delta\varepsilon_r = 1$ is used. The perturbation steps for the shape parameters are $\Delta t = 0.005a =$ 0.174 mm, $\Delta r = 0.003a = 0.1044$ mm, and $\Delta s = 0.005\lambda = 0.218$ mm.

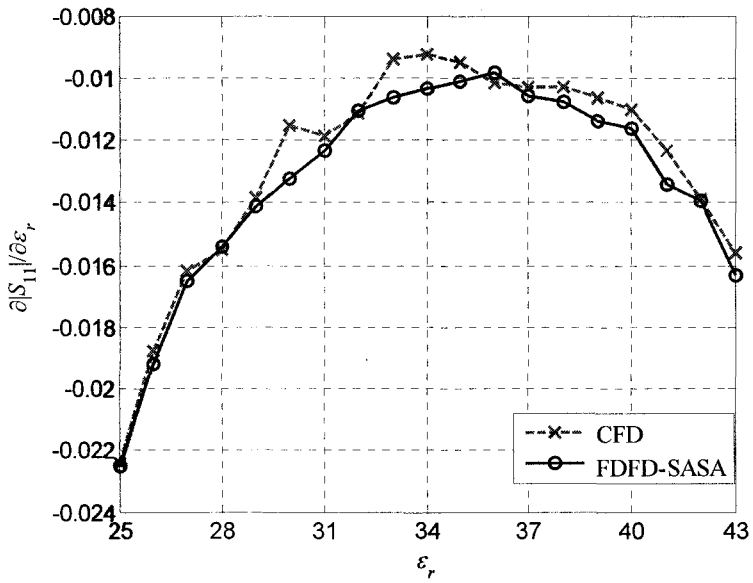

Figure 3.5 Derivatives of $|S_{11}|$ at 6.88 GHz with respect to ε_r, when $t/a = 0.2$, $r/a = \mathbf{0.06}$, and $s/\lambda = 0.32$.

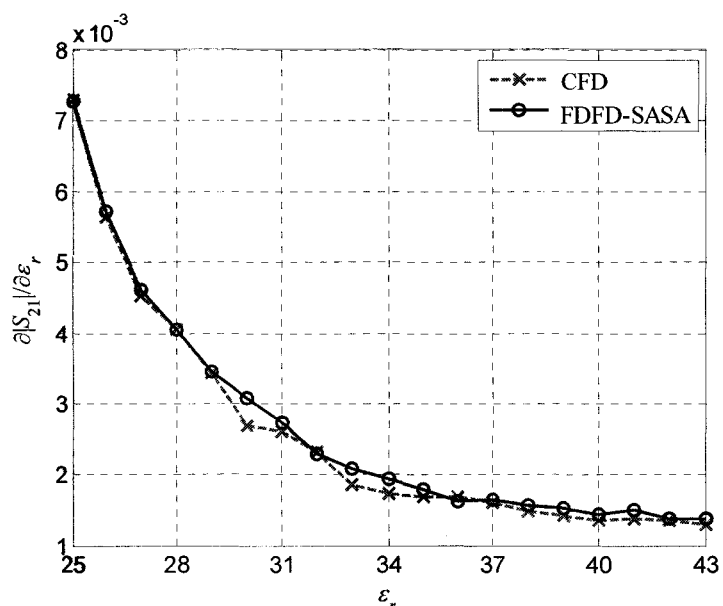

Figure 3.6 Derivatives of $|S_{21}|$ at 6.88 GHz with respect to ε_r, when $t/a = 0.2$, $r/a = \mathbf{0.06}$, and $s/\lambda = 0.32$.

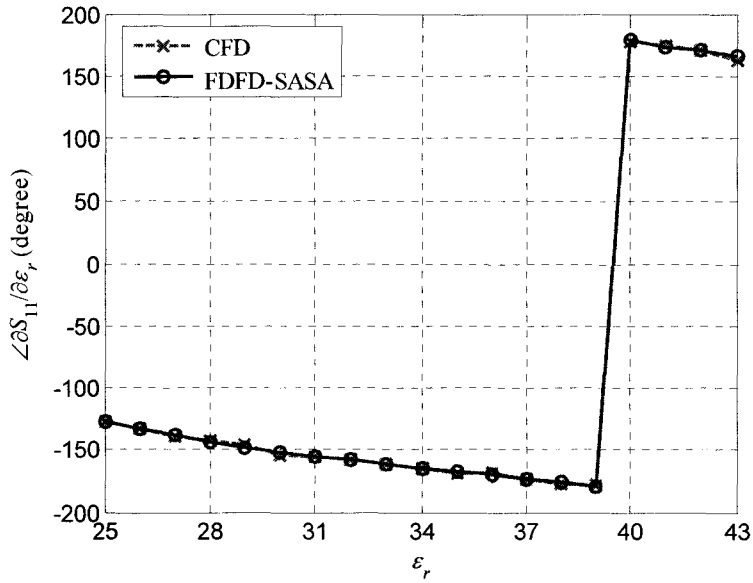

Figure 3.7 Derivatives of $\angle S_{11}$ at 6.88 GHz with respect to ε_r, when $t/a = 0.2$, $r/a = 0.06$, and $s/\lambda = 0.32$.

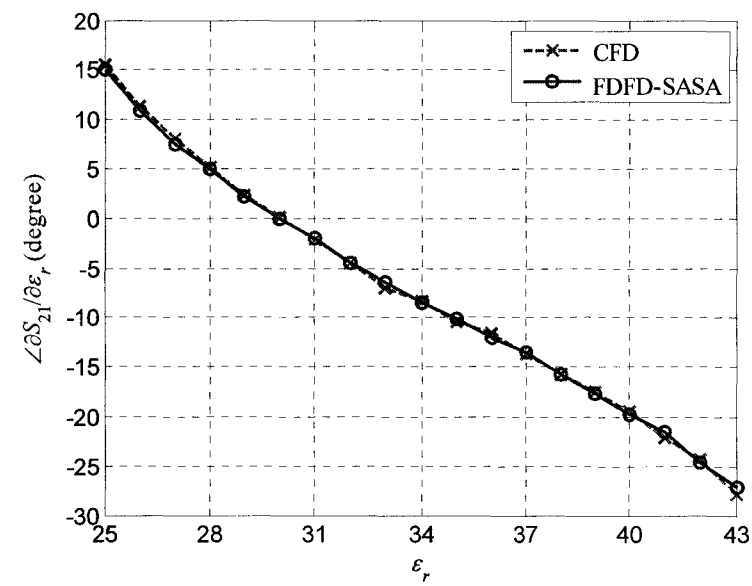

Figure 3.8 Derivatives of $\angle S_{21}$ at 6.88 GHz with respect to ε_r, when $t/a = 0.2$, $r/a = 0.06$, and $s/\lambda = 0.32$.

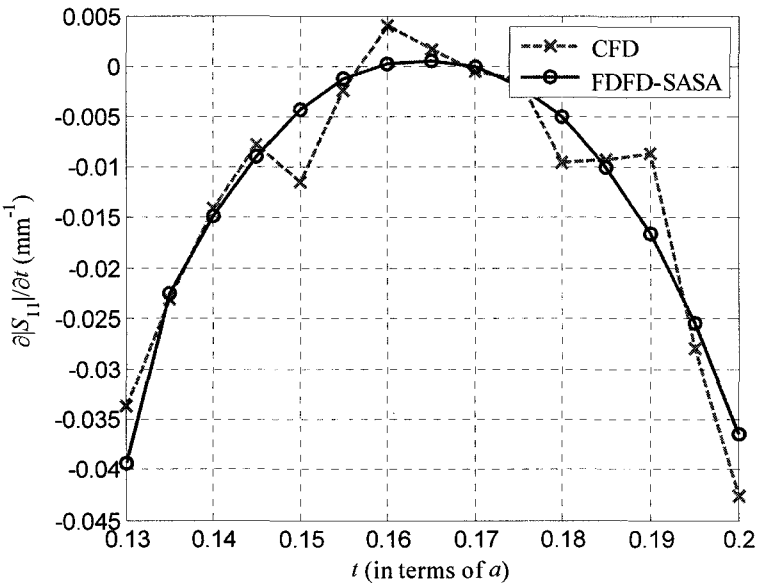

Figure 3.9 Derivatives of $|S_{11}|$ at 6.88 GHz with respect to t, when $\varepsilon_r = 38.5$, $r/a = 0.06$, and $s/\lambda = 0.32$.

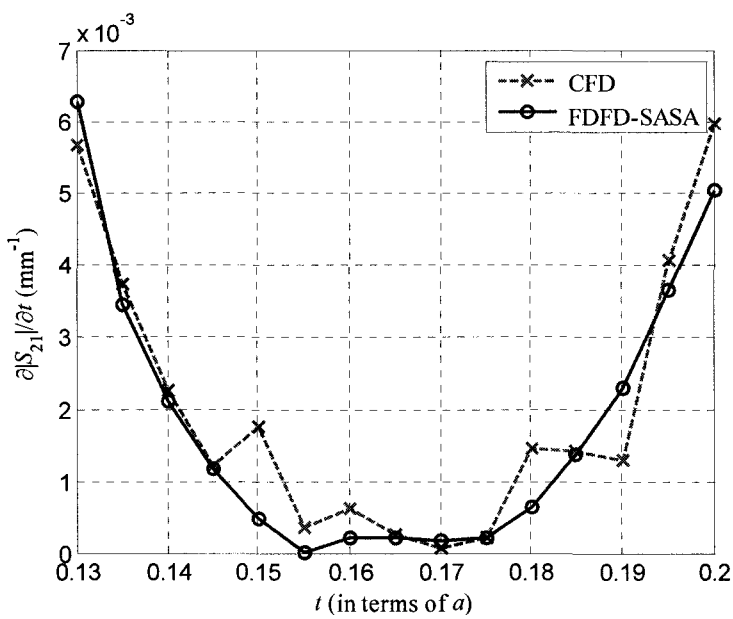

Figure 3.10 Derivatives of $|S_{21}|$ at 6.88 GHz with respect to t, when $\varepsilon_r = 38.5$, $r/a = 0.06$, and $s/\lambda = 0.32$.

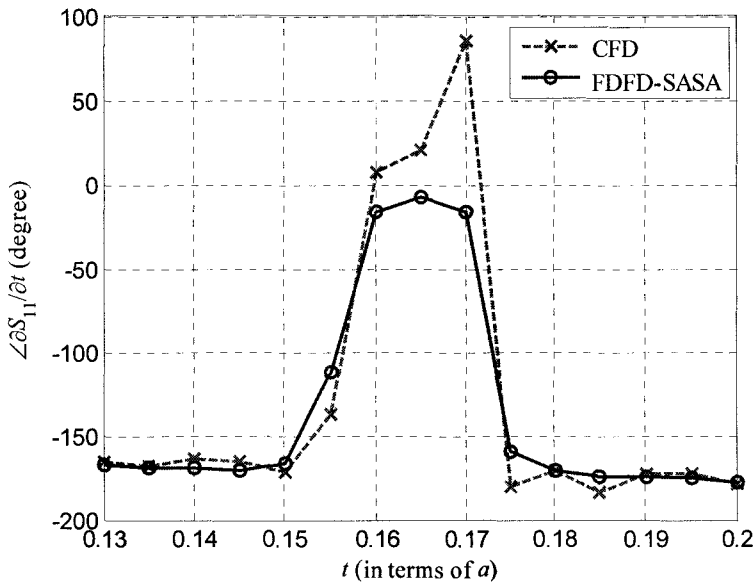

Figure 3.11 Derivatives of $\angle S_{11}$ at 6.88 GHz with respect to t, when $\varepsilon_r = 38.5$, $r/a = 0.06$, and $s/\lambda = 0.32$.

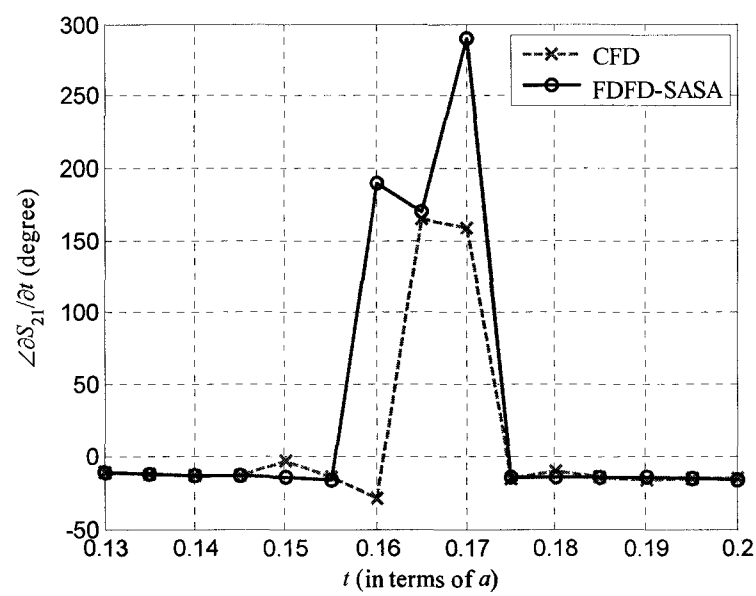

Figure 3.12 Derivatives of $\angle S_{21}$ at 6.88 GHz with respect to t, when $\varepsilon_r = 38.5$, $r/a = 0.06$, and $s/\lambda = 0.32$.

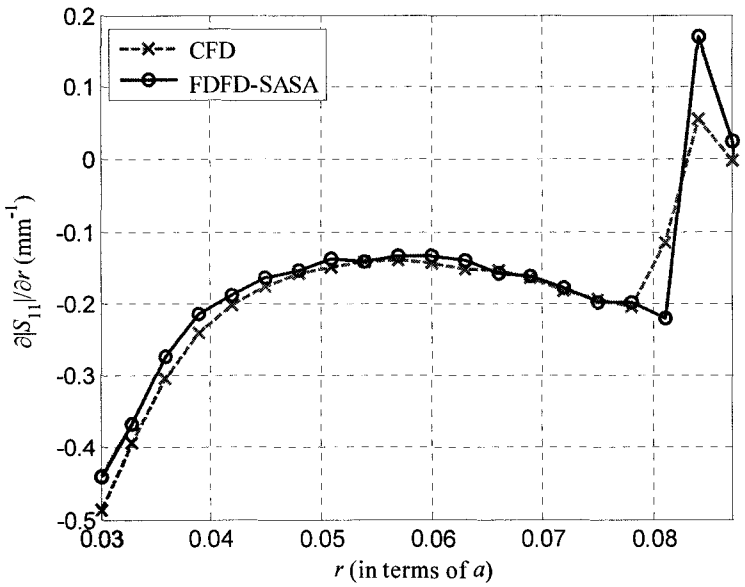

Figure 3.13 Derivatives of $|S_{11}|$ at 6.88 GHz with respect to r, when $\varepsilon_r = 38.5$, $t/a = 0.2$, and $s/\lambda = 0.32$.

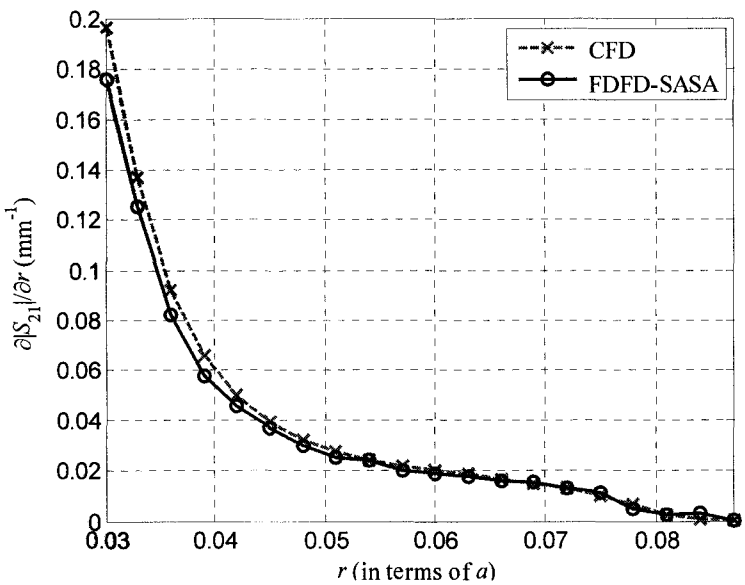

Figure 3.14 Derivatives of $|S_{21}|$ at 6.88 GHz with respect to r, when $\varepsilon_r = 38.5$, $t/a = 0.2$, and $s/\lambda = 0.32$.

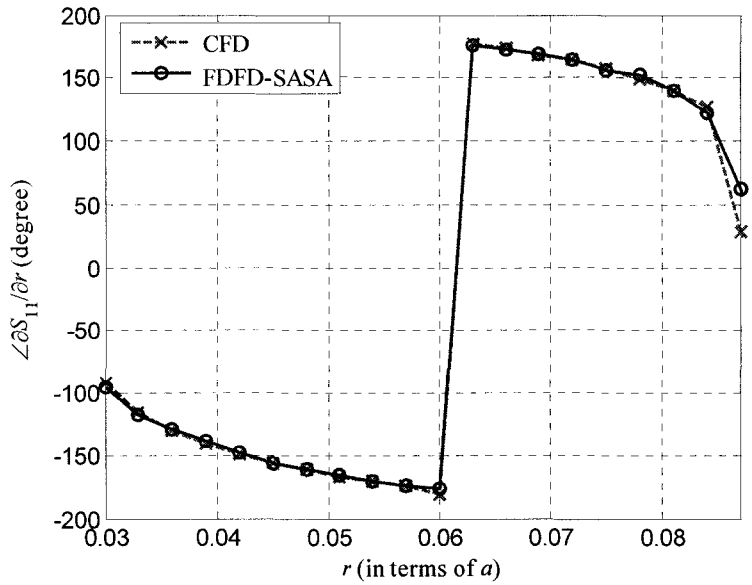

Figure 3.15 Derivatives of $\angle S_{11}$ at 6.88 GHz with respect to r, when $\varepsilon_r = 38.5$, $t/a = 0.2$, and $s/\lambda = 0.32$.

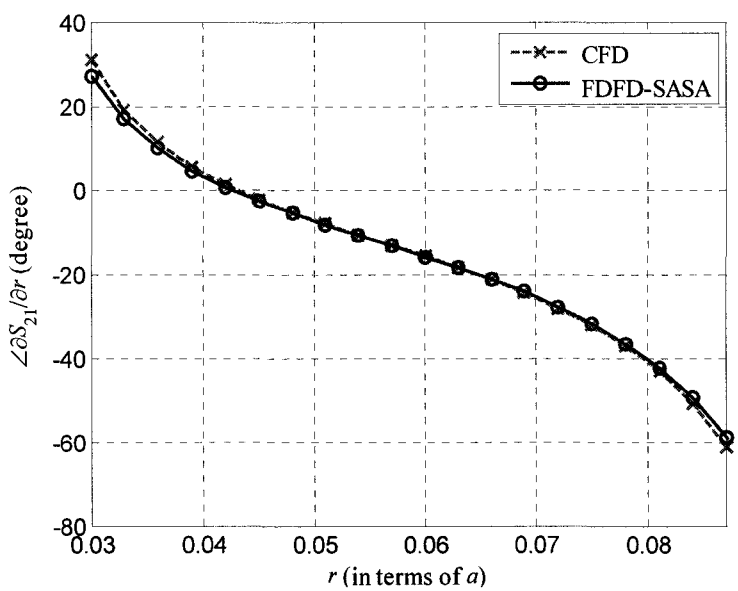

Figure 3.16 Derivatives of $\angle S_{21}$ at 6.88 GHz with respect to r, when $\varepsilon_r = 38.5$, $t/a = 0.2$, and $s/\lambda = 0.32$.

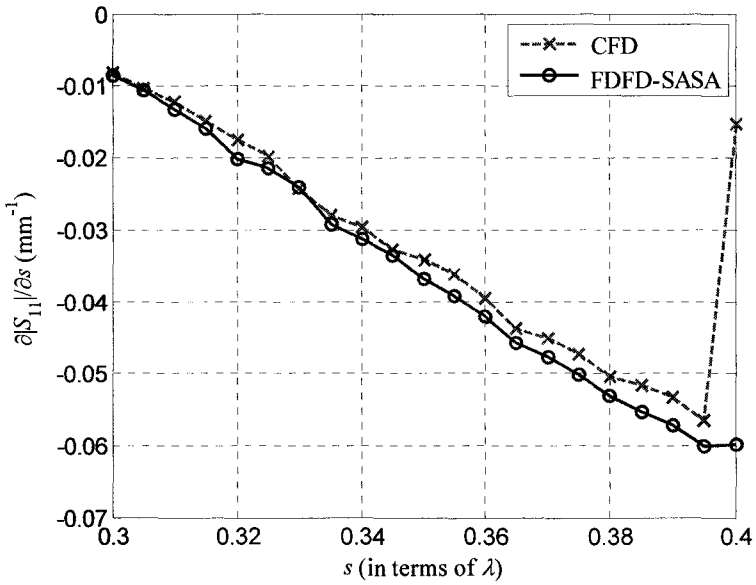

Figure 3.17 Derivatives of $|S_{11}|$ at 6.88 GHz with respect to s, when $\varepsilon_r = 38.5$, $t/a = 0.2$, and $r/a = 0.06$.

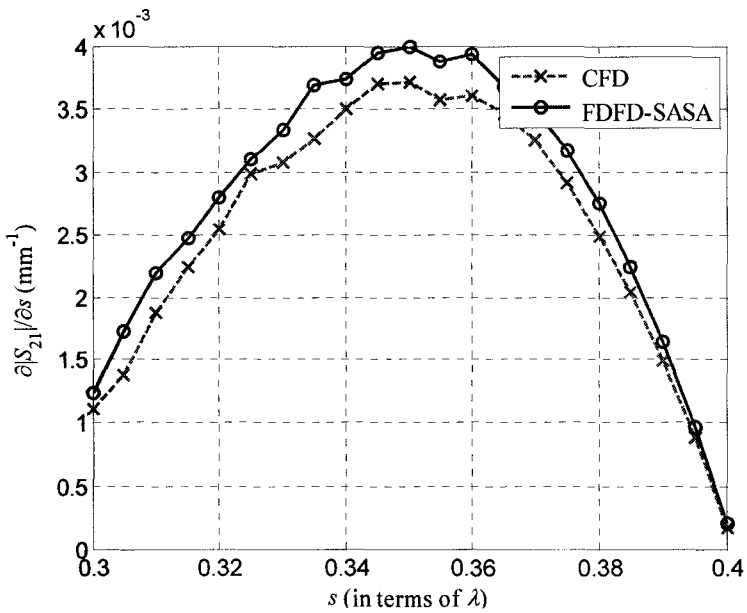

Figure 3.18 Derivatives of $|S_{21}|$ at 6.88 GHz with respect to s, when $\varepsilon_r = 38.5$, $t/a = 0.2$, and $r/a = 0.06$.

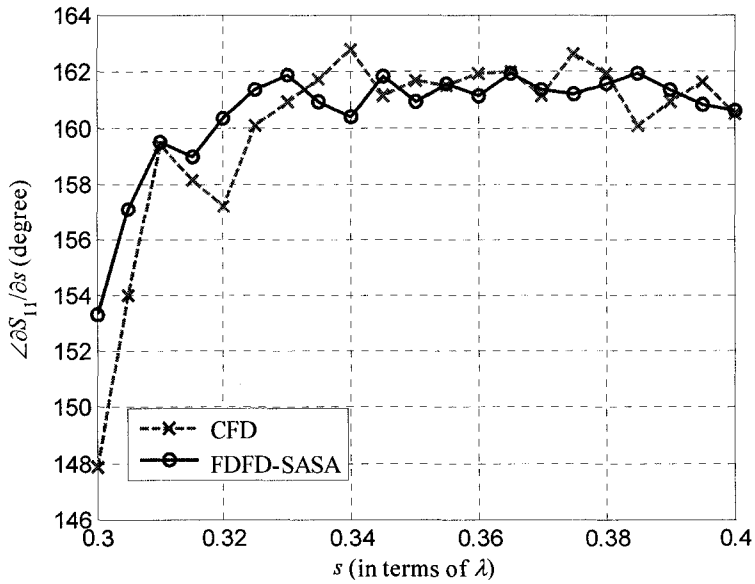

Figure 3.19 Derivatives of $\angle S_{11}$ at 6.88 GHz with respect to s, when $\varepsilon_r = 38.5$, $t/a = 0.2$, and $r/a = 0.06$.

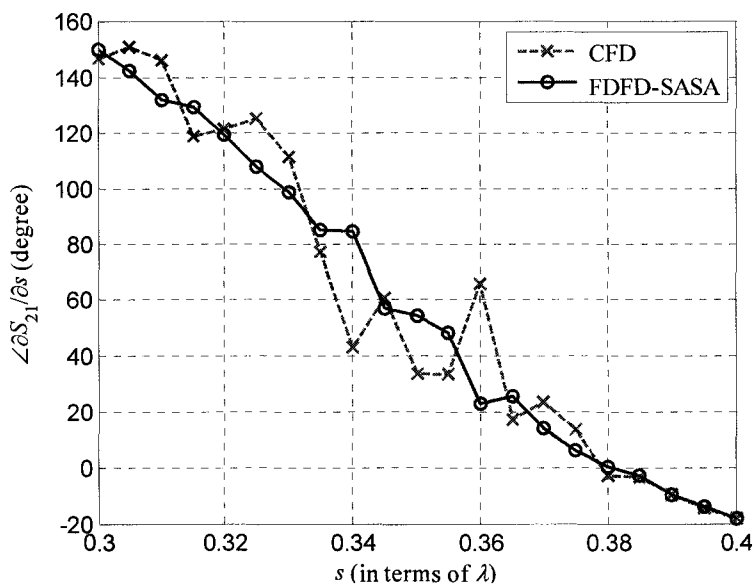

Figure 3.20 Derivatives of $\angle S_{21}$ at 6.88 GHz with respect to s, when $\varepsilon_r = 38.5$, $t/a = 0.2$, and $r/a = 0.06$.

We observe that the agreement between the CFD and the FDFD-SASA curves is generally very good. Also, we see that the FDFD-SASA derivatives are smoother functions of the respective parameters, which is an indication that they suffer less from the numerical noise of the EM simulation [1], [5] than the CFD curves. In fact, the CFD curves plotted here as a reference were carefully selected after adjusting each parameter perturbation for minimal numerical noise. The lack of reliability in the finite-difference estimates of the response derivatives using numerical solutions is a well known problem. There are two reasons: (1) if the perturbation Δp_n is too small, the response from the simulator is almost the same as before. Hence, the difference between the two responses, the nominal and the perturbed one, may be reduced to just numerical noise; and (2) if the perturbation Δp_n is too large, especially when the objective function is highly nonlinear, the CFD result may miss this nonlinear property. Thus, we never know how to choose Δp_n properly for response-level finite differences. At the same time, the FDFD-SASA needs no prior adjustment of any parameter perturbation since the system-coefficient derivatives always use: (1) analytical expressions for material parameters, and (2) finite-difference coefficients obtained with an assumed perturbation of one grid cell for shape parameters. Our sensitivity formulas indicate that, if the field solutions in the computational domain are accurate enough, the accuracy of the sensitivity computation is guaranteed.

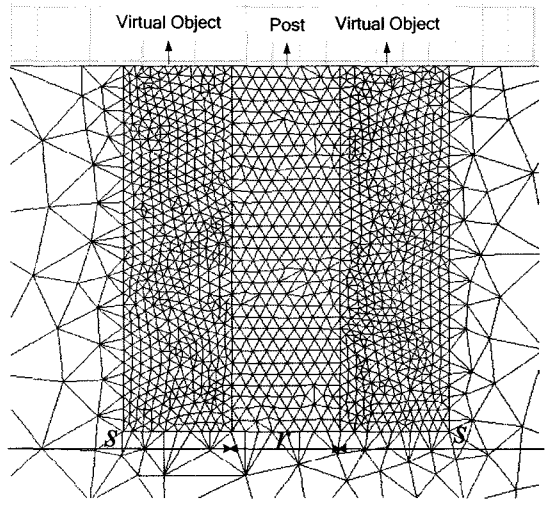

Figure 3.21 Mesh plot for the designable parameter s around one post showing two virtual objects, which enforce fine mesh on both sides of the post.

For electrically large objects, if the mesh edge is less than $\lambda/20$, where λ is the wavelength at the frequency of the simulation, the accuracy of the field solution is sufficient. In this situation, Ansoft HFSS can guarantee the accuracy of the field solution if the solution convergence error is set properly, e.g., equal to 0.005. However, for electrically small objects with dimensions much smaller than $\lambda/20$, in order to guarantee the accuracy of the field solution at the perturbation grid points, we have to employ mesh control and enforce mesh-edge length so that each dimension of the small objects has several mesh edges, not just one. We may also need to insert some virtual objects so that we exercise the mesh control in the necessary areas only. This is because mesh control may slow down the simulation. In our *H*-plane filter analysis, for example, the response is very sensitive with respect to the s parameter. Besides, we need to export the field

solution around the posts to compute the derivatives. We insert two virtual objects, and force the mesh edge to be equal to $r_0/8$ as shown in figure 3.21.

Theoretically, the FDFD-SASA results are not affected by the assumed perturbation if the field solution is accurate. However, when we use our defined FD grid to export the field solution from the field calculator, Ansoft HFSS employs interpolation. If our assumed perturbation is too small, noise is introduced into the field solution, and finally into the sensitivity results. Thus, it is important to know the optimal choice for the step size of the sensitivity grid as compared to the local FEM mesh-edge length.

Figures 3.22 and 3.33 plot the derivatives with respect to s with different FD grid. Here, we denote with $\Delta\chi$ the local mesh-edge length in Ansoft HFSS, while Δh is the FD grid step. We set $\Delta\chi = r_0/8$. Figures 3.22 and 3.33 illustrate that the FDFD-SASA results are convergent. The optimal FD grid step size is roughly equal to one mesh-edge length of the local FEM mesh, i.e., Δh should be set as $\Delta h \approx \Delta\chi$.

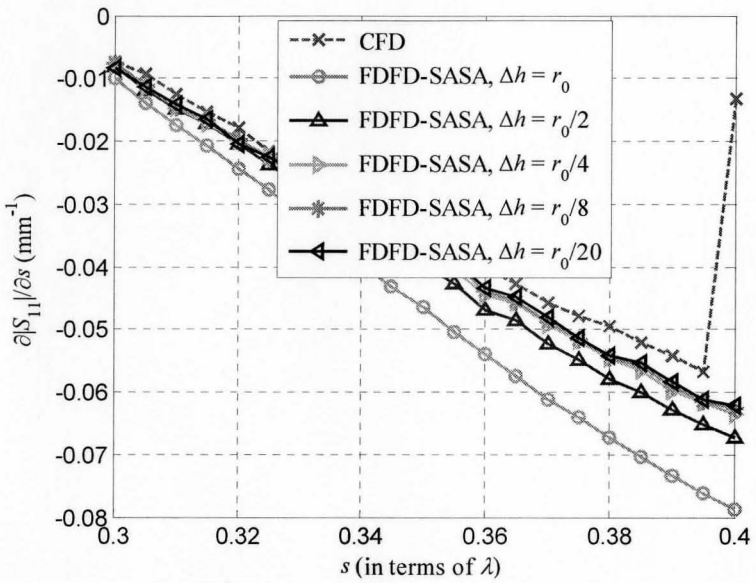

Figure 3.22 Derivatives of $|S_{11}|$ at 6.88 GHz with respect to s with different FD grid step size Δh.

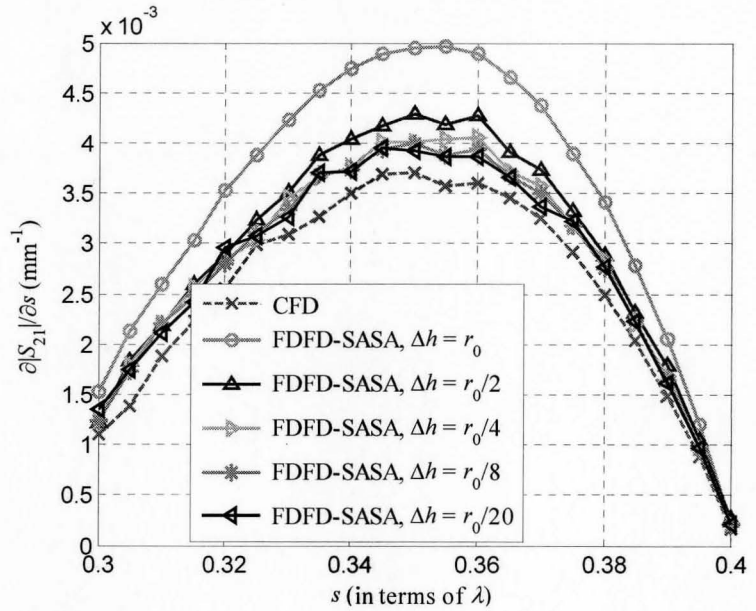

Figure 3.23 Derivatives of $|S_{21}|$ at 6.88 GHz with respect to s with different FD grid step size Δh.

3.5.3 3-D example: dielectric-resonator antenna

We use an aperture-coupled rectangular dielectric-resonator antenna (DRA) [12] as a 3-D example. Figure 3.24 shows the structure and the nominal values for all parameters. This DRA is fed by a microstrip line through an aperture in the ground plane. Figure 3.25 shows its return loss at the nominal state. The designable parameters can be the length a, the width b, and the height c of the dielectric resonator, the width w_a and the length l_a of the coupled aperture, as well as the length of the open-end stub l_s. Here, to validate our sensitivity analysis in dielectric structures, we consider four parameters: one material parameter ε_{r1}, and three shape parameters a, b, and c.

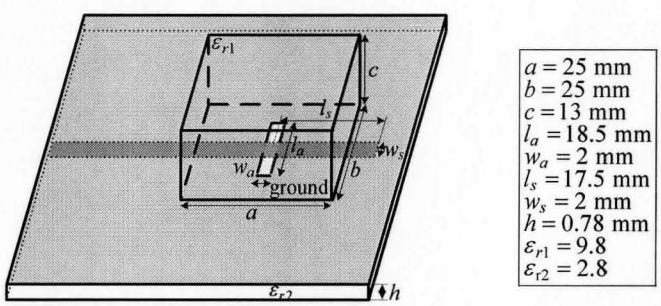

Figure 3.24 The structure of the dielectric-resonator antenna.

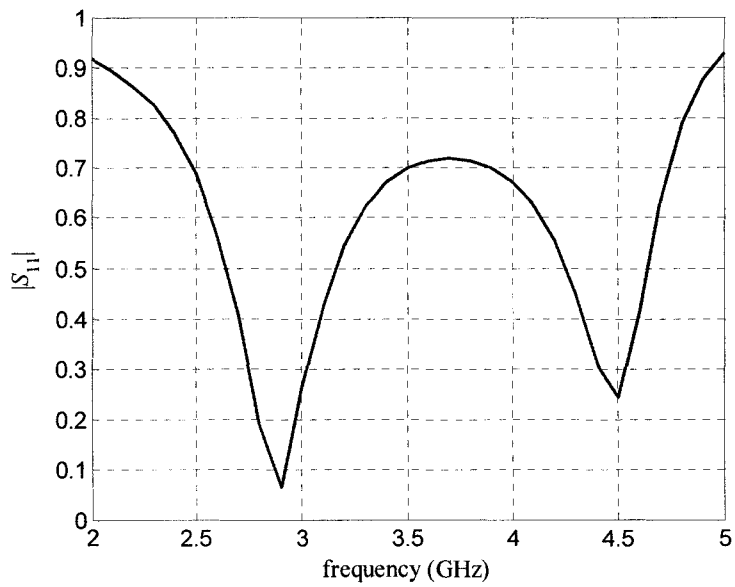

Figure 3.25 The return loss of the dielectric-resonator antenna.

The derivatives of the return loss with respect to ε_{r1}, a, b, and c are plotted in figures 3.26 to 3.33. Figures 3.26 to 3.29 are obtained at 3.5 GHz. Figures 3.30 to 3.33 show the derivatives of the return loss over a frequency sweep from 2 GHz to 5 GHz. We use CFD results as our reference curves to validate the FDFD-SASA results. We select the FD perturbation steps carefully as: $\Delta\varepsilon_{r1} = 0.5$, $\Delta a = 0.5$ mm, $\Delta b = 0.5$ mm, and $\Delta c = 0.5$ mm. In FDFD-SASA, the assumed perturbation step for each parameter is set to be equal to the shortest edge of the mesh generated by Ansoft HFSS inside the dielectric resonator. Again, very good agreement is observed between the CFD and the FDFD-SASA results.

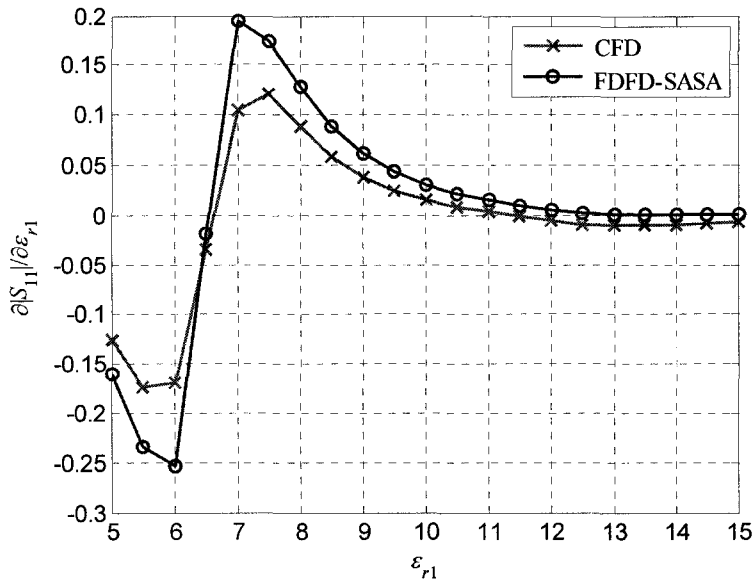

Figure 3.26 Derivatives of $|S_{11}|$ at 3.5 GHz with respect to ε_{r1}, when $a = 25$ mm, $b = 25$ mm, and $c = 13$ mm.

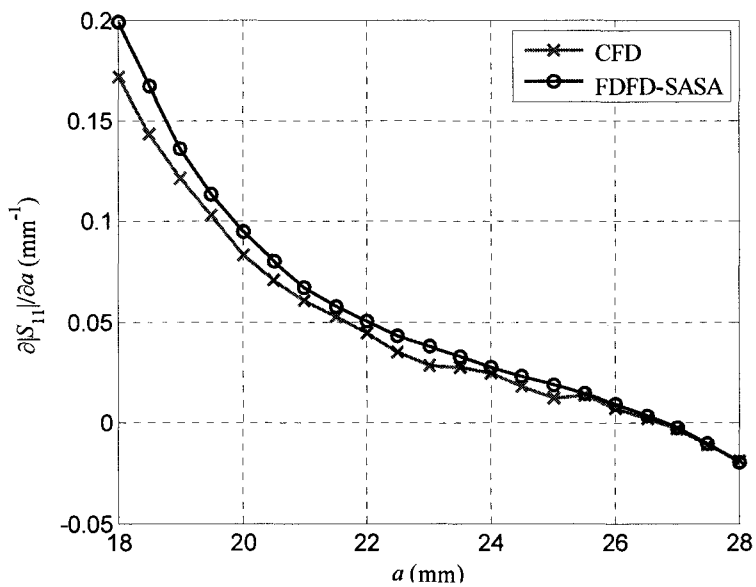

Figure 3.27 Derivatives of $|S_{11}|$ at 3.5 GHz with respect to a, when $\varepsilon_{r1} = 9.8$, $b = 25$ mm, and $c = 13$ mm.

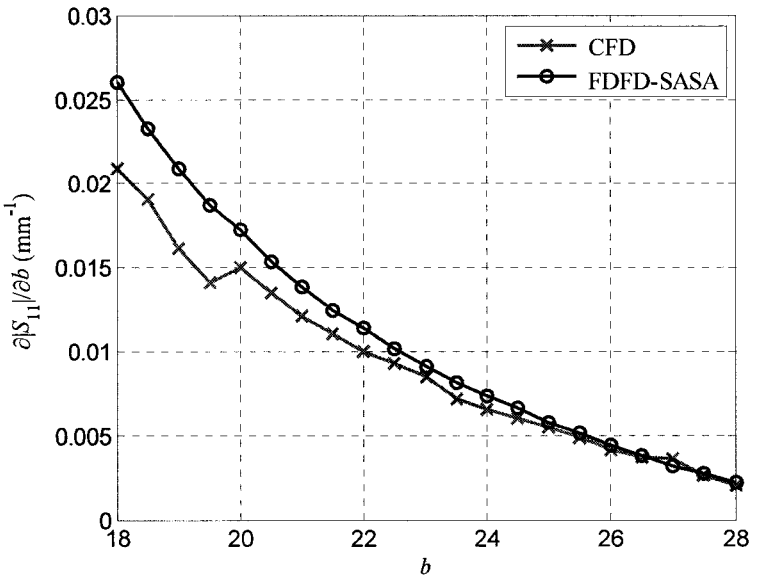

Figure 3.28 Derivatives of $|S_{11}|$ at 3.5 GHz with respect to b, when $\varepsilon_{r1} = 9.8$, $a = 25$ mm, and $c = 13$ mm.

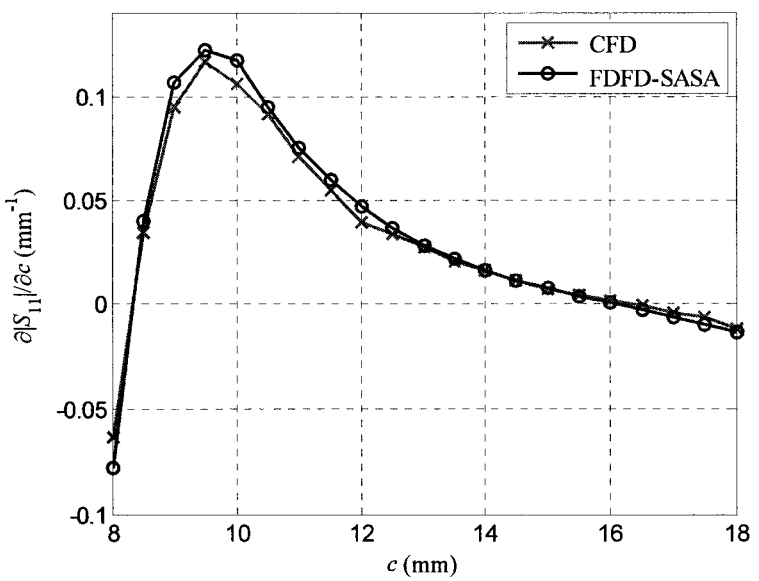

Figure 3.29 Derivatives of $|S_{11}|$ at 3.5 GHz with respect to c, when $\varepsilon_{r1} = 9.8$, $a = 25$ mm, and $b = 25$ mm.

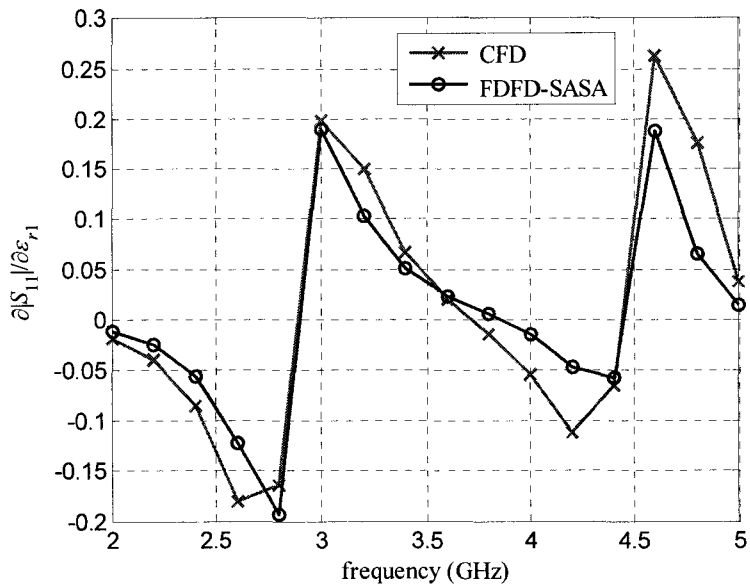

Figure 3.30 Derivatives of $|S_{11}|$ with respect to ε_{r1} over a frequency band when $\varepsilon_{r1}=9.8$, $a=25$ mm, $b=25$ mm, and $c=13$ mm.

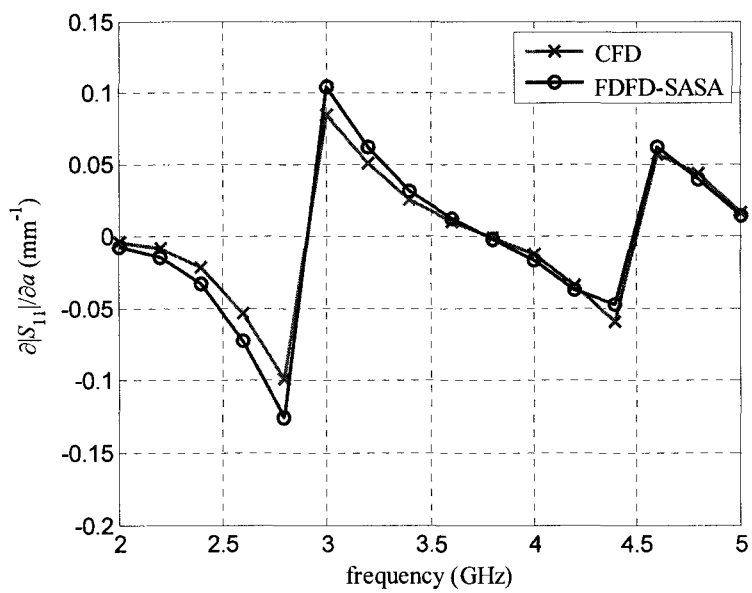

Figure 3.31 Derivatives of $|S_{11}|$ with respect to a over a frequency band when $\varepsilon_{r1}=9.8$, $a=25$ mm, $b=25$ mm, and $c=13$ mm.

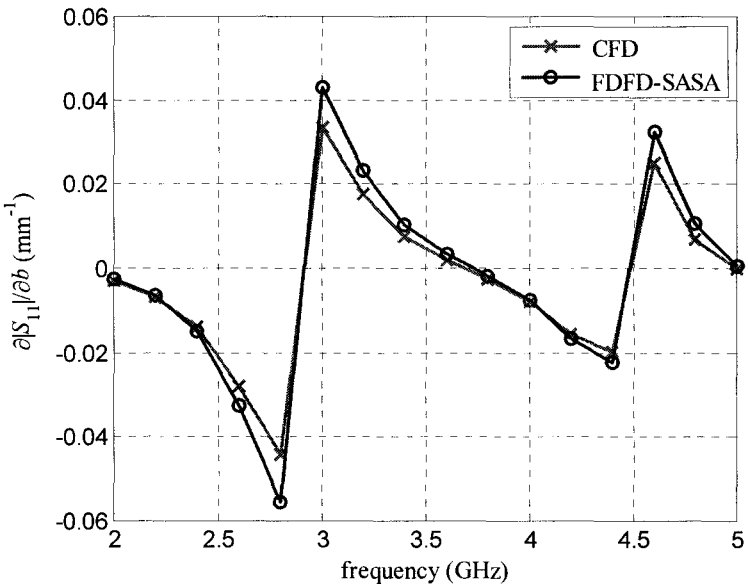

Figure 3.32 Derivatives of $|S_{11}|$ with respect to b over a frequency band when $\varepsilon_{r1}=9.8$, $a=25$ mm, $b=25$ mm, and $c=13$ mm.

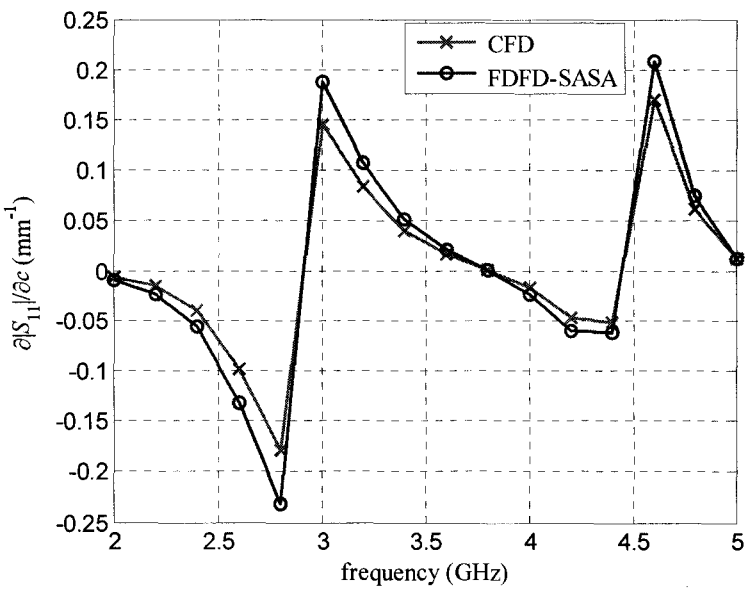

Figure 3.33 Derivatives of $|S_{11}|$ with respect to c over a frequency band when $\varepsilon_{r1}=9.8$, $a=25$ mm, $b=25$ mm, and $c=13$ mm.

3.6 Implementation of the FDFD-SASA for Metallic Structures (Background) [13]

Compared to dielectric structures, the difference of the implementation for metallic structures appears in: (1) the computation of the derivatives of the system residual, and (2) the locations of the perturbation grid points. The implementations for assumed metallization and de-metallization are different [4]. In this section, we outline the implementation of the FDFD-SASA for 3-D metallic structures. The simpler 2-D implementation is explained in [4], [13].

3.6.1 Metallization

If the assumed perturbation causes metallization of cells, the system residual derivative reduces to [4]

$$\frac{\Delta_n R(\mathbf{E}_j)}{\Delta_n p} = \frac{\Delta_n \mathbb{C}^2 \mathbf{E}_j}{\Delta_n p}. \tag{3.66}$$

As illustrated in section 3.2, the x-component of $\mathbb{C}^2\mathbf{E}$ with Yee-cell grid can be expressed as

$$(\mathbb{C}^2\mathbf{E})_x = h_y^2 D_{yy}^{\mu} E_x + h_z^2 D_{zz}^{\mu} E_x - h_y h_x D_{yx}^{\mu} E_y - h_z h_x D_{zx}^{\mu} E_z. \tag{3.67}$$

Let us now illustrate how to compute $(\mathbb{C}^2\mathbf{E})_x$ on a central-node FD grid. We assume that the relative permeability $\mu_r = 1$ for simplicity.

Using the central finite differences, the second-order derivative $\partial^2 E_x / \partial y^2$ at point (0, 0, 0) is obtained as

$$\frac{\partial^2 E_x}{\partial y^2} \approx \frac{1}{\Delta y^2}\left[E_x^{(0,1,0)} + E_x^{(0,-1,0)} - 2E_x^{(0,0,0)}\right] = \frac{1}{\Delta y^2} \cdot D_{yy}E_x. \tag{3.68}$$

The dots in figure 3.34 represent the locations of the points required to compute $D_{yy}E_x$.

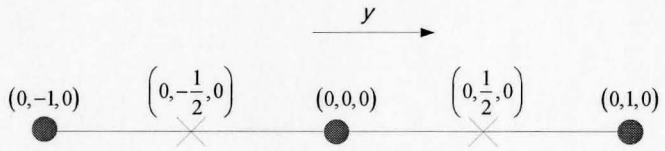

Figure 3.34 Point locations for the calculation of $D_{yy}E_x$.

The second-order mixed derivative $\partial^2 E_y / \partial y \partial x$ at point (0, 0, 0) can be written as

$$\frac{\partial^2 E_y}{\partial y \partial x} \approx \frac{1}{2\Delta x}\left[f^{(1,0,0)} - f^{(-1,0,0)}\right], \tag{3.69}$$

where

$$f^{(1,0,0)} \approx \frac{1}{2\Delta y}\left[E_y^{(1,1,0)} - E_y^{(1,-1,0)}\right] \tag{3.70}$$

$$f^{(-1,0,0)} \approx \frac{1}{2\Delta y}\left[E_y^{(-1,1,0)} - E_y^{(-1,-1,0)}\right]. \tag{3.71}$$

Hence, we have

$$\frac{\partial^2 E_y}{\partial y \partial x} \approx \frac{1}{4\Delta x \Delta y}\left[E_y^{(1,1,0)} + E_y^{(-1,-1,0)} - E_y^{(-1,1,0)} - E_y^{(1,-1,0)}\right] = \frac{1}{4\Delta x \Delta y} \cdot D_{yx}E_y. \tag{3.72}$$

The dark dots in figure 3.35 represent the locations of the points required to compute $D_{yx}E_y$.

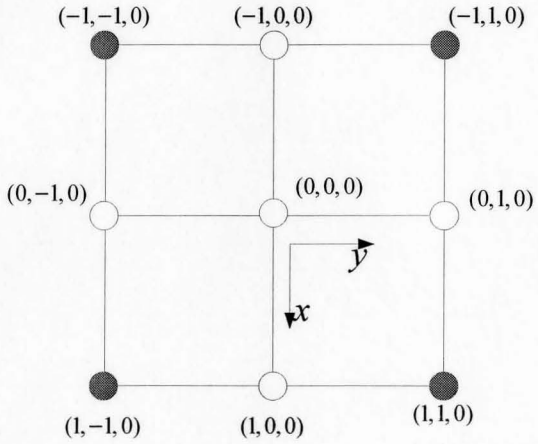

Figure 3.35 Point locations for the calculation of $D_{yx}E_y$.

Following similar procedures, the general expressions for the $\mathbb{C}^2\mathbf{E}$ components on a central-node FD grid are:

$$\left(\mathbb{C}^2\mathbf{E}\right)_x = h_y^2 D_{yy}E_x + h_z^2 D_{zz}E_x - \frac{1}{4}\left[h_y h_x D_{yx}E_y + h_z h_x D_{zx}E_z\right] \tag{3.73}$$

$$\left(\mathbb{C}^2\mathbf{E}\right)_y = h_z^2 D_{zz}E_y + h_x^2 D_{xx}E_y - \frac{1}{4}\left[h_z h_y D_{zy}E_z + h_x h_y D_{xy}E_x\right] \tag{3.74}$$

$$\left(\mathbb{C}^2\mathbf{E}\right)_z = h_x^2 D_{xx}E_z + h_y^2 D_{yy}E_z - \frac{1}{4}\left[h_x h_z D_{xz}E_x + h_y h_z D_{yz}E_y\right], \tag{3.75}$$

where

$$D_{yy}E_x\big|_{i,j,k} = E_x^{i,j+1,k} + E_x^{i,j-1,k} - 2E_x^{i,j,k} \tag{3.76}$$

$$D_{zz}E_x\big|_{i,j,k} = E_x^{i,j,k+1} + E_x^{i,j,k-1} - 2E_x^{i,j,k} \tag{3.77}$$

$$D_{xy}E_y\big|_{i,j,k} = E_y^{i+1,j+1,k} + E_y^{i-1,j-1,k} - E_y^{i-1,j+1,k} - E_y^{i+1,j-1,k} \tag{3.78}$$

$$D_{zx}E_z\big|_{i,j,k} = E_z^{i+1,j,k+1} + E_z^{i-1,j,k-1} - E_z^{i-1,j,k+1} - E_z^{i+1,j,k-1} \tag{3.79}$$

$$D_{zz}E_y\big|_{i,j,k} = E_y^{i,j,k+1} + E_y^{i,j,k-1} - 2E_y^{i,j,k} \tag{3.80}$$

$$D_{xx}E_y\big|_{i,j,k} = E_y^{i+1,j,k} + E_y^{i-1,j,k} - 2E_y^{i,j,k} \tag{3.81}$$

$$D_{zy}E_z\big|_{i,j,k} = E_z^{i,j+1,k+1} + E_z^{i,j-1,k-1} - E_z^{i,j-1,k+1} - E_z^{i,j+1,k-1} \tag{3.82}$$

$$D_{xy}E_x\big|_{i,j,k} = E_x^{i+1,j+1,k} + E_x^{i-1,j-1,k} - E_x^{i+1,j-1,k} - E_x^{i-1,j+1,k} \tag{3.83}$$

$$D_{xx}E_z\big|_{i,j,k} = E_z^{i+1,j,k} + E_z^{i-1,j,k} - 2E_z^{i,j,k} \tag{3.84}$$

$$D_{yy}E_z\big|_{i,j,k} = E_z^{i,j+1,k} + E_z^{i,j-1,k} - 2E_z^{i,j,k} \tag{3.85}$$

$$D_{xz}E_x\big|_{i,j,k} = E_x^{i+1,j,k+1} + E_x^{i-1,j,k-1} - E_x^{i+1,j,k-1} - E_x^{i-1,j,k+1} \tag{3.86}$$

$$D_{yz}E_y\big|_{i,j,k} = E_y^{i,j+1,k+1} + E_y^{i,j-1,k-1} - E_y^{i,j+1,k-1} - E_y^{i,j-1,k+1}. \tag{3.87}$$

In figure 3.36, we assume that the shape parameter p_n is perturbed by one cell, i.e., $\Delta p_n = \Delta x$. This shift causes the metallization of the light-gray cells. **E** field at those locations jumps from some nonzero value to zero, which means the coefficients of $\mathbb{C}^2\mathbf{E}_j$ at the black dots, which are related to the field at the white dots, change from some nonzero value to zero. $(\mathbf{E}_k)_n$ at the black dots is also needed. Here, one-to-one mapping is used as described in section 3.5.1. We approximate $(\mathbf{E}_k)_n$ at the black dots of figure 3.36a by $\mathbf{E}_k$ at the crosses of figure 3.36b, i.e., $(\mathbf{E}_k)_n^{i,j,k} = \mathbf{E}_k{}^{i-1,j,k}$.

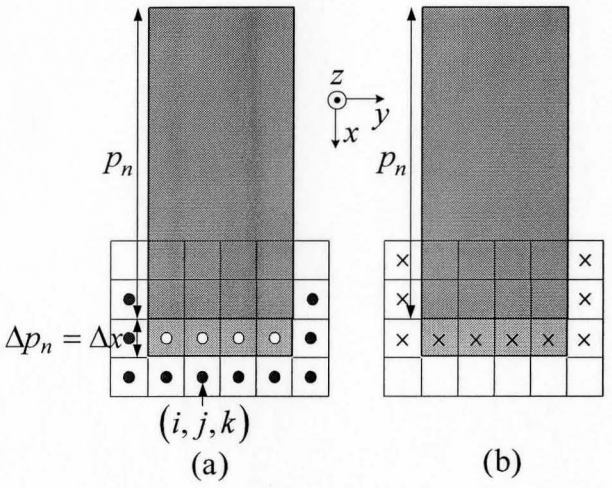

Figure 3.36 Illustration of the perturbation grid points for the shape parameter p_n of a metallic post: (a) locations (the black dots) where the double-curl operator $\mathbb{C}^2$ is affected due to metallization at the white dots—$\mathbf{E}_j$ is recorded at the white dots; (b) locations where $\mathbf{E}_k$ is recorded and mapped to $(\mathbf{E}_k)_n$ at the black dots of figure 3.36a.

Let us illustrate the computation of $\Delta_n \mathbb{C}^2 \mathbf{E}_j$ at the black dots with a sampling point (i, j, k) shown in figure 3.36a. The x component of $\mathbb{C}^2\mathbf{E}$ is

$$\left(\mathbb{C}^2\mathbf{E}\right)_x = h_y^2 D_{yy} E_x + h_z^2 D_{zz} E_x - \frac{1}{4}\left[h_y h_x D_{yx} E_y + h_z h_x D_{zx} E_z\right] \tag{3.88}$$

where

$$D_{yy}E_x\big|_{i,j,k} = E_x^{i,j+1,k} + E_x^{i,j-1,k} - 2E_x^{i,j,k} \tag{3.89}$$

$$D_{zz}E_x\big|_{i,j,k} = E_x^{i,j,k+1} + E_x^{i,j,k-1} - 2E_x^{i,j,k} \tag{3.90}$$

$$D_{xy}E_y\big|_{i,j,k} = E_y^{i+1,j+1,k} + E_y^{i-1,j-1,k} - E_y^{i-1,j+1,k} - E_y^{i+1,j-1,k} \tag{3.91}$$

$$D_{zx}E_z\big|_{i,j,k} = E_z^{i+1,j,k+1} + \underline{E_z^{i-1,j,k-1}} - \underline{E_z^{i-1,j,k+1}} - E_z^{i+1,j,k-1}. \tag{3.92}$$

The y component of $\mathbb{C}^2\mathbf{E}$ is

$$\left(\mathbb{C}^2\mathbf{E}\right)_y = h_z^2 D_{zz}E_y + h_x^2 D_{xx}E_y - \frac{1}{4}\left[h_z h_y D_{zy}E_z + h_x h_y D_{xy}E_x\right] \tag{3.93}$$

where

$$D_{zz}E_y\big|_{i,j,k} = E_y^{i,j,k+1} + E_y^{i,j,k-1} - 2E_y^{i,j,k} \tag{3.94}$$

$$D_{xx}E_y\big|_{i,j,k} = E_y^{i+1,j,k} + \underline{E_y^{i-1,j,k}} - 2E_y^{i,j,k} \tag{3.95}$$

$$D_{zy}E_z\big|_{i,j,k} = E_z^{i,j+1,k+1} + E_z^{i,j-1,k-1} - E_z^{i,j-1,k+1} - E_z^{i,j+1,k-1} \tag{3.96}$$

$$D_{xy}E_x\big|_{i,j,k} = E_x^{i+1,j+1,k} + \underline{E_x^{i-1,j-1,k}} - E_x^{i+1,j-1,k} - \underline{E_x^{i-1,j+1,k}}. \tag{3.97}$$

The z component of $\mathbb{C}^2\mathbf{E}$ is

$$\left(\mathbb{C}^2\mathbf{E}\right)_z = h_x^2 D_{xx}E_z + h_y^2 D_{yy}E_z - \frac{1}{4}\left[h_x h_z D_{xz}E_x + h_y h_z D_{yz}E_y\right], \tag{3.98}$$

where

$$D_{xx}E_z\big|_{i,j,k} = E_z^{i+1,j,k} + \underline{E_z^{i-1,j,k}} - 2E_z^{i,j,k} \tag{3.99}$$

$$D_{yy}E_z\big|_{i,j,k} = E_z^{i,j+1,k} + E_z^{i,j-1,k} - 2E_z^{i,j,k} \tag{3.100}$$

$$D_{xz}E_x\big|_{i,j,k} = E_x^{i+1,j,k+1} + \underline{E_x^{i-1,j,k-1}} - E_x^{i+1,j,k-1} - \underline{E_x^{i-1,j,k+1}} \tag{3.101}$$

$$D_{yz}E_y\big|_{i,j,k} = E_y^{i,j+1,k+1} + E_y^{i,j-1,k-1} - E_y^{i,j+1,k-1} - E_y^{i,j-1,k+1}. \tag{3.102}$$

Underlined terms indicate where the field solutions must be set to zero at the nth perturbed state. There, the coefficients of $\mathbb{C}^2\mathbf{E}$ related to the underlined terms

jump from some value to zero. Since $\Delta_n \mathbb{C}^2 \mathbf{E}_j = \left(\mathbb{C}^2 \mathbf{E}_j\right)_n - \mathbb{C}^2 \mathbf{E}_j$, it is in effect equal to the sum of all underlined terms with a minus sign. Thus, $\Delta_n \mathbb{C}^2 \mathbf{E}_j$ at the black dots is entirely dependent on the original field solution $\mathbf{E}_j$ at the white dots. Notice figure 3.36 only shows a 2-D cut of the 3-D structure. The field we exported in figure 3.36 extends along z dimension.

In our implementation, we generate an auxiliary field solution $\mathbf{E}_a$ where the field solution at the metalized cells (the white dots in figure 3.36a) is equal to $\mathbf{E}_j$ and zero elsewhere. Taking the $\mathbb{C}^2$ on $\mathbf{E}_a$ produces $-\Delta_n \mathbb{C}^2 \mathbf{E}_j$, i.e., $\Delta_n \mathbb{C}^2 \mathbf{E}_j = -\mathbb{C}^2 \mathbf{E}_a$.

Assume that the full-wave analysis of the nominal problem has been carried out. With the metallization assumption, the *S*-parameter sensitivity derivatives can be computed according to the following steps.

Step 1: Compute the self-adjoint constant as described in section 3.5.1.

Step 2: Record $\mathbf{E}_j$ at the white dots and $\mathbf{E}_k$ at the crosses of figure 3.36. $\mathbf{E}_k$ at the crosses approximates $\left(\mathbf{E}_k\right)_n$ at the black dots.

Step 3: Generate the auxiliary solution $\mathbf{E}_a$ from $\mathbf{E}_j$. Compute $\mathbb{C}^2 \mathbf{E}_a$ with (3.73) to (3.87). Obtain the system residual differences at the black dots as $\Delta_n R(\mathbf{E}_j) = \Delta_n \mathbb{C}^2 \mathbf{E}_j = -\mathbb{C}^2 \mathbf{E}_a$.

Step 4: Compute the *S*-parameter sensitivity derivatives with the discretized formula (3.65).

3.6.2 De-metallization

If the assumed perturbation causes de-metallization of cells, the system residual derivative reduces to [4]

$$\frac{\Delta_n R(\mathbf{E}_j)}{\Delta_n p} = -\frac{\Delta_n \mathbf{G}_j}{\Delta_n p}. \tag{3.103}$$

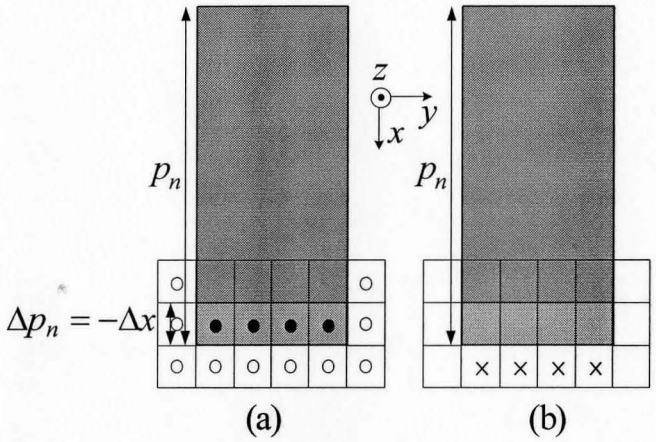

Figure 3.37 Illustration of the perturbation grid points for the shape parameters p_n of a metallic post: (a) locations (the black dots) where $\mathbf{G}_j$ is affected due to de-metallization— $\mathbf{E}_j$ is recorded at the white dots; (b) locations where $\mathbf{E}_k$ is recorded and mapped to $(\mathbf{E}_k)_n$ at the black dots of figure 3.37a.

We assume a decrease of p_n in figure 3.37, which creates a de-metalized region, the light-gray cells. Before the perturbation, $\mathbf{E}_j = 0$ is imposed at the black dots, because this region belongs to the metallic object. The induced current there is

$$\beta \cdot \mathbf{J}_j^{\text{ind}} = \mathbb{C}^2 \mathbf{E}_j . \tag{3.104}$$

After the perturbation, the above induced current does not exist. Hence, we have

$$\Delta_n R(\mathbf{E}_j) = -\Delta_n \left(\beta \cdot \mathbf{J}_j^{\text{ind}} \right) = \beta \cdot \mathbf{J}_j^{\text{ind}} - \left(\beta \cdot \mathbf{J}_j^{\text{ind}} \right)_n = \beta \cdot \mathbf{J}_j^{\text{ind}} = \mathbb{C}^2 \mathbf{E}_j . \tag{3.105}$$

The computation of $\Delta_n R(\mathbf{E}_j) = \mathbb{C}^2 \mathbf{E}_j$ involves the field $\mathbf{E}_j$ at both white and black dots, but the field at the black dots is zero. $(\mathbf{E}_k)_n$ at the black dots is also needed, but it is obtained from $\mathbf{E}_k$ at the crosses in figure 3.37b. Same as in figure 3.36, the field we exported in figure 3.37 extends along z dimension.

The *S*-parameter sensitivity derivatives in the case of de-metallization can be obtained with the following steps.

Step 1: Compute the self-adjoint constant as described in section 3.5.1.

Step 2: Record $\mathbf{E}_j$ at the white dots of figure 3.37a and $\mathbf{E}_k$ at the crosses of figure 3.37b. As before, $\mathbf{E}_k$ at the crosses approximates $(\mathbf{E}_k)_n$ at the black dots.

Step 3: Compute the system residual differences at the black dots using (3.105).

Step 4: Compute the *S*-parameter sensitivity derivatives with the discretized formula (3.65).

3.7 Implementation of the FDFD-SASA for Infinitesimally Thin Metallic Structures

Metallic sheet is a special case of the metallic structure which is infinitesimally thin. The shape has two dimensions, but the sensitivity calculations with respect to the designable parameters involve field solution in three dimensions. Similarly to the case of 3-D metallic structures, the implementations for metallization and de-metallization are different.

3.7.1 Metallization

The assumed perturbation in figure 3.38 creates the metallization of the light-gray rectangle. In figure 3.38, E_x and E_y at the light-gray area must be set to zero after perturbation.

$\mathbb{C}^2\mathbf{E}_j$ at the black dots of three layers—the middle layer is in the plane of the metallic sheet plane—is affected by the change of the coefficients of those related to E_x and E_y at the metalized rectangular, which jump from some nonzero value to zero. $(\mathbf{E}_k)_n$ at the black dots of these three layers is also needed. It is approximated by $\mathbf{E}_k$ at the crosses, i.e., $(\mathbf{E}_k)_n^{i,j,k} = \mathbf{E}_k{}^{i-1,j,k}$.

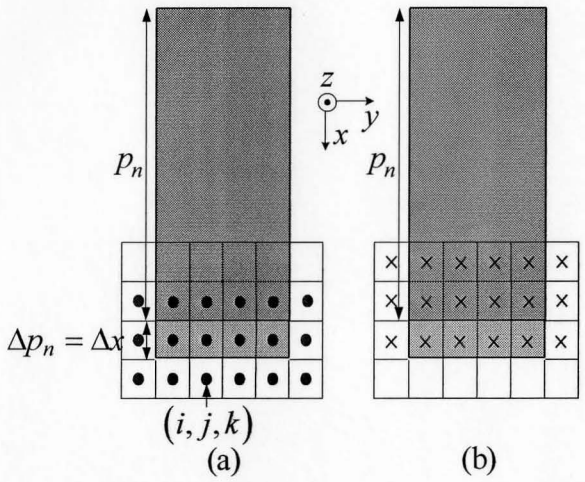

Figure 3.38 Illustration of the perturbation grid points for the shape parameter p_n of a metallic sheet: (a) locations (the black dots of all three layers) where the double-curl operator $\mathbb{C}^2$ is affected due to metallization—the x and y components of $\mathbf{E}_j$ are recorded at the black dots of the light-gray rectangular; (b) locations (the crosses of all three layers) where $\mathbf{E}_k$ is recorded and mapped to $(\mathbf{E}_k)_n$ at the black dots of figure 3.38a.

If we illustrate the computation of $\Delta_n \mathbb{C}^2 \mathbf{E}_j$ at the black dots of all three layers with a sampling point (*i, j, k*), we should be aware that the terms containing E_z do not go to zero in contrast to the 3-D case. Only the coefficients of $\mathbb{C}^2 \mathbf{E}_j$ related to the tangential **E** components at the light-gray rectangular jump from some nonzero value to zero. Hence, $\Delta_n \mathbb{C}^2 \mathbf{E}_j$ at the black dots of the three layers is entirely dependent on the tangential components of $\mathbf{E}_j$ at the light-gray rectangular. Similarly, as in 3-D metallic structures, we create an auxiliary field solution $\mathbf{E}_a$, whose tangential components of the field at the black dots of the

light-gray rectangular is equal to the tangential components of $\mathbf{E}_j$ and zero elsewhere. Taking the operator of $\mathbb{C}^2$ on $\mathbf{E}_a$ gives the system residual difference as $\Delta_n R(\mathbf{E}_j) = \Delta_n \mathbb{C}^2 \mathbf{E}_j = -\mathbb{C}^2 \mathbf{E}_a$.

The implementation of *S*-parameter sensitivity derivatives can be described in the following steps.

Step 1: Compute the self-adjoint constant as described in section 3.5.1.

Step 2: Record the tangential components of $\mathbf{E}_j$ at the black dots of the light-gray rectangular and $\mathbf{E}_k$ at the crosses of all three layers. $\mathbf{E}_k$ at the crosses approximates $(\mathbf{E}_k)_n$ at the black dots.

Step 3: Generate the auxiliary field $\mathbf{E}_a$ using $\mathbf{E}_j$. Compute $\mathbb{C}^2\mathbf{E}_a$ and obtain the system residual differences at the black dots of all three layers as $\Delta_n R(\mathbf{E}_j) = \Delta_n \mathbb{C}^2 \mathbf{E}_j = -\mathbb{C}^2 \mathbf{E}_a$.

Step 4: Compute the *S*-parameter sensitivity derivatives with the discretized formula (3.65).

3.7.2 De-metallization

The assumed perturbation in figure 3.39 creates a de-metalized region, the light-gray rectangular. Before the perturbation, $E_x = 0$ and $E_y = 0$ are imposed at the light-gray area. The induced current exists there, which is

$$\left(\beta \cdot \mathbf{J}_j^{\text{ind}}\right)_x = \left(\mathbb{C}^2\mathbf{E}\right)_x, \left(\beta \cdot \mathbf{J}_j^{\text{ind}}\right)_y = \left(\mathbb{C}^2\mathbf{E}\right)_y, \left(\beta \cdot \mathbf{J}_j^{\text{ind}}\right)_z = 0. \qquad (3.106)$$

After the perturbation, the above induced current vanishes. Similar to (3.105), we have

$$\Delta_n R_x(\mathbf{E}_j) = \left(\mathbb{C}^2\mathbf{E}_j\right)_x,\ \Delta_n R_y(\mathbf{E}_j) = \left(\mathbb{C}^2\mathbf{E}_j\right)_y,\ \Delta_n R_z(\mathbf{E}_j) = 0. \qquad (3.107)$$

The computation of $\Delta_n R(\mathbf{E}_j)$ at the light-gray rectangular involves $\mathbf{E}_j$ at the black dots of three layers—the middle layer is in the plane of the metallic sheet plane. $(\mathbf{E}_k)_n$ at the black dots of the light-gray rectangular is also needed. It is approximated by $\mathbf{E}_k$ at the crosses, i.e., $(\mathbf{E}_k)_n^{i,j,k} = \mathbf{E}_k{}^{i+1,j,k}$.

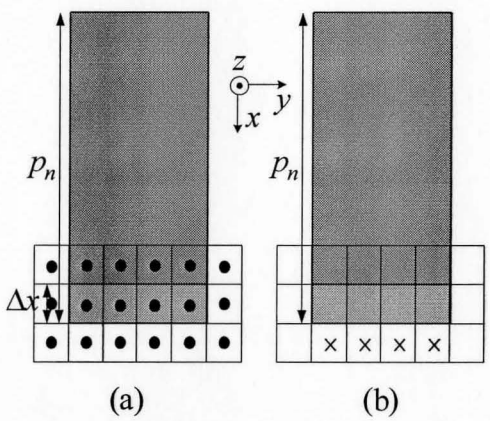

Figure 3.39 Illustration of the perturbation grid points for the shape parameters p_n of a metallic sheet: (a) locations (the black dots of the light-gray rectangular) where $\mathbf{G}_j$ is affected due to de-metallization—$\mathbf{E}_j$ are recorded at the black dots of all three layers; (b) locations (the crosses at the metallic sheet plane) where $\mathbf{E}_k$ is recorded and mapped to $(\mathbf{E}_k)_n$ at the black dots of the light-gray rectangular in figure 3.39a.

With the de-metallization assumption, the computation of *S*-parameter sensitivity derivatives can be obtained with the following steps.

Step 1: Compute the self-adjoint constant as described in section 3.5.1.

Step 2: Record $\mathbf{E}_j$ at black dots of all three layers and $\mathbf{E}_k$ at the crosses of the metallic sheet plane shown in figure 3.39. $\mathbf{E}_k$ at the crosses approximates $(\mathbf{E}_k)_n$ at the black dots of the light-gray rectangular.

Step 3: Compute $\Delta_n R(\mathbf{E}_j)$ at the black dots of the light-gray rectangular using (3.107).

Step 4: Compute the *S*-parameter sensitivity derivatives with the discretized formula (3.65).

3.7.3 Example: dielectric-resonator antenna

We use the same validation example as in section 3.43—an dielectric-resonator antenna shown in figure 3.24. Here, the designable parameter is l_a. Figure 3.40 plots the derivatives of the return loss with respect to l_a over a frequency sweep from 2 GHz to 5 GHz. The FD perturbation step is $\Delta l_a = 0.5$ mm. The assumed FDFD-SASA perturbation grid step is 0.5 mm, which is equal to one FEM mesh edge around the aperture. A good agreement between the CFD and the FDFD-SASA results is observed in figure 3.40.

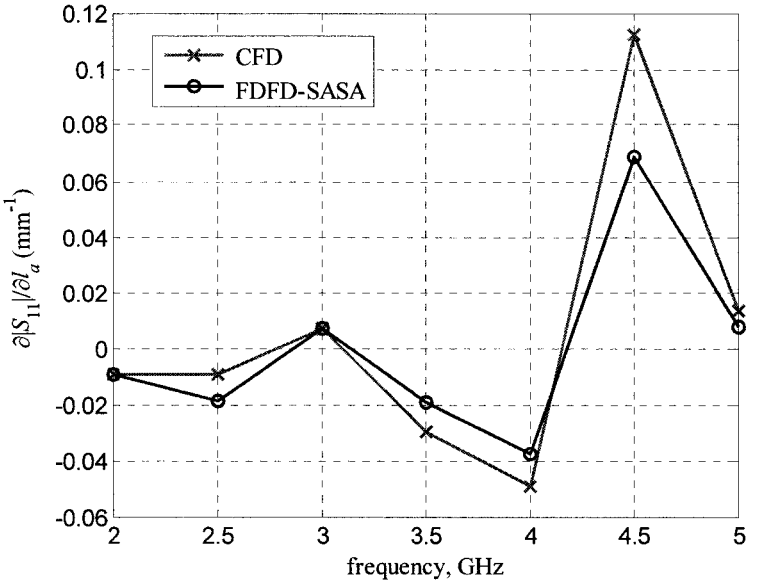

Figure 3.40 Derivatives of $|S_{11}|$ with respect to l_a over a frequency band when $l_a = 19$.

3.8 References

[1] N. K. Nikolova, J. Zhu, D. Li, M. Bakr, and J. Bandler, "Sensitivities of network parameters with electromagnetic frequency domain simulators," *IEEE Trans. Microwave Theory Tech.*, vol. 54, pp. 670-681, Feb. 2006.

[2] X. Zhu, A. Hasib, and N. K. Nikolova, "Electromagnetic sensitivity analysis of scattering parameters based on the FDFD method," *Int. Symp. on Signals, Systems, and Electronics (ISSSE 2007)*, pp. 165-168, Jul.-Aug. 2007.

[3] N. K. Nikolova, A. Hasib, and X. Zhu, "Independent sensitivity solver based on the frequency domain finite difference method," *The 24th Int. Review of Progress in Applied Computational Electromagnetics (ACES 2008)*, pp. 1024-1029, Mar.-Apr. 2008.

[4] N. K. Nikolova, H. W. Tam, M. H. Bakr, "Sensitivity analysis with the FDTD method on structured grids," *IEEE Trans. Microwave Theory Tech.*, vol. 52, pp. 1207-1216, Apr. 2004.

[5] N. K. Nikolova, Ying Li, Yan Li, and M. H. Bakr, "Sensitivity analysis of scattering parameters with electromagnetic time-domain simulators," *IEEE Trans. Microwave Theory Tech.*, vol. 54, pp. 1589-1610, Apr. 2006.

[6] Ansoft HFSS ver. 10, Ansoft Corporation, 225 West Station Square Drive, Suite 200, Pittsburgh, PA 15219, USA, 2006, www.ansoft.com.

[7] Ansoft HFSS ver. 11, Ansoft Corporation, 225 West Station Square Drive, Suite 200, Pittsburgh, PA 15219, USA, 2007, www.ansoft.com.

[8] M. H. Bakr and N. K. Nikolova, "An adjoint variable method for frequency domain TLM problems with conducting boundaries," *IEEE Microwave and Wireless Components Letters,* vol. 13, pp. 408-410, Nov. 2003.

[9] Y. Song, Ying Li, N. K. Nikolova, and M.H. Bakr, "Self-adjoint sensitivity analysis of lossy dielectric structures with electromagnetic time-domain simulators," *Int. J. of Numerical Modelling: Electronic Networks, Devices and Fields,* vol. 21, pp. 117-132, Oct. 2007.

[10] Y. Song and N.K. Nikolova, "Central-node approach for accurate self-adjoint sensitivity analysis of dielectric structures," *IEEE MTT-S Int. Microwave Symposium*, pp. 895-898, Jun. 2007.

[11] L. Minakova and L. Rud, "Spectral approach to the synthesis of the waveguide bandstop filters based on dielectric rectangular posts," *Int. Conference on Mathematical Methods in Electromagnetic Theory MMET*, pp. 479-481, Sep. 2000.

[12] D. Yau and N. V. Shuley, "A moment method analysis of an aperture coupled rectangular dielectric resonator antenna," *IEEE AP-S/URSI Int. Antennas Propagation Symposium*, vol. 2, pp. 858-861, Jul. 1999.

[13] A. Hasib, *Sensitivity Analysis for Design Optimization of Metallic Microwave Structures with the Finite-difference Frequency-domain Method*, M.A.Sc. Thesis, Department of Electrical and Computer Engineering, McMaster University, Hamilton, ON, Canada, Apr. 2008.

Chapter 4

MICROWAVE DESIGN OPTIMIZATION USING SENSITIVITY ANALYSIS

4.1 Introduction

According to whether Jacobian information is used, the optimization algorithms can be categorized as gradient-based or non-gradient ones [1]. The gradient-based optimization algorithms, such as quasi-Newton, sequential quadratic programming (SQP) or trust-region methods, require the objective function Jacobians and/or Hessians in addition to the objective function itself. With a good initial design, a gradient-based optimization algorithm is expected to converge much faster than a non-gradient one. Its drawback is that a global optimal point is not guaranteed, neither is its convergence. It is because gradient-based optimization algorithms search for a local minimum. The non-gradient optimization algorithms, such as the traditional pattern search [2],

genetic and particle swarm algorithms [2], [3], or some neural-network based algorithms [4], require only the objective function. They are preferred when there is little information about the initial design. Their drawback is the need for a large number of system analyses. Since full-wave electromagnetic (EM) simulations are very time-consuming, such approaches are not practical. Besides, microwave engineers can often obtain acceptable initial designs based on their knowledge and experience. Hence, gradient-based optimization algorithms are often preferred in practical EM design problems.

The efficiency of a successful gradient-based optimization process mainly relies on two factors [5]: (1) the number of the iterations required to achieve the convergence, and (2) the number of system analysis per iteration. The first factor depends largely on the nature of the algorithm, the proper formulation of the objective function, and the accuracy of the response Jacobians and/or Hessians. The second one depends on the method used to compute the Jacobians and/or Hessians. The finite-difference (FD) approximation at the response level requires at least one additional system analysis for each designable parameter. This is inefficient especially when the number of designable parameters is large. In contrast, the finite-difference frequency-domain self-adjoint sensitivity analysis (FDFD-SASA), as illustrated in Chapter 3, can yield the responses and their Jacobians with only one system analysis.

In this chapter, we apply the FDFD-SASA to microwave design optimization with two validation examples: an *H*-plane dielectric-resonator filter

and a dielectric-resonator antenna. Section 4.2 introduces the optimization problem for filter/antenna design. Section 4.3 presents two validation examples, including the comparison of the convergence and the time requirements of the FDFD-SASA and the FD method.

4.2 The Optimization Problem [6]

The design problem is defined as

$$\boldsymbol{p}^* = \arg\min_{\boldsymbol{p}} F(\boldsymbol{R}(\boldsymbol{p})) \tag{4.1}$$

where $\boldsymbol{R}$ is the vector of M responses, $\boldsymbol{p}$ is the vector of designable parameters, and $\boldsymbol{p}^*$ is the optimal solution which minimizes the objective function F. In our examples, the M responses are the S-parameter magnitudes evaluated at select frequencies where design goals specify lower (L) or upper (U) bounds for the responses. F is defined as $F = \max\{e_1,\ldots,e_M\}$, where the error e_m, $m = 1,\ldots,M$ ($M = M_L + M_U$), is $e_m = L_m - R_m$, $m = 1,\ldots,M_L$, in the case of a lower bound, and $e_m = R_m - U_m$, $m = M_L + 1,\cdots,M$, for an upper bound.

4.3 Examples

We apply the FDFD-SASA to the design of two microwave devices: an H-plane dielectric-resonator filter and a dielectric-resonator antenna. For each component, we perform two independent optimization processes. One is carried

out with the Jacobians provided by the FDFD-SASA, the other by enforcing response-level calculation of the Jacobians via forward finite differences (FFD). In both examples, we use Madsen's minimax optimization algorithm [7] which requires response Jacobians. Besides, this algorithm employs a trust region.

4.3.1 *H*-plane dielectric-resonator filter [6]

The layout of the bandstop filter is shown in figure 3.3. The relative permittivity of all dielectric posts is set as 38.5. The designable parameters are $p = [t\ r\ s]^T$. The design specifications are

$$\begin{aligned} |S_{21}| &\geq 0.8 \text{ for } 4.4 \leq f \leq 5.0 \text{ GHz} \\ |S_{21}| &\leq 0.2 \text{ for } 5.0 \leq f \leq 5.5 \text{ GHz} \\ |S_{21}| &\geq 0.8 \text{ for } 5.75 \leq f \leq 6.35 \text{ GHz.} \end{aligned} \tag{4.2}$$

The initial design is $\boldsymbol{p}^{(0)} = [5.5\ 2.0\ 14]^T$ mm. Its insertion loss is shown in figure 4.1. We set the initial trust region as $r^{(0)} = 0.1 \| \boldsymbol{p}^{(0)} \|$, which is recommended for highly nonlinear problems. The response Jacobians are provided by our FDFD-SASA solver. Its uniform central-node grid is set as $\Delta h = 0.5$ mm, which is roughly equal to the shortest edge length of the finite-element method (FEM) mesh generated by Ansoft HFSS [8] in and around the dielectric posts.

For comparison, we perform a separate optimization process where we do not use our sensitivity solver and enforce response-level calculation of the

Jacobians via FFD. This optimization process is an example of current practices in EM design optimization. When computing the FFD Jacobians, one has to carefully choose the amounts of perturbation Δp_n. Otherwise, the FFD Jacobians are inaccurate and may result in trapping the optimization in a local minimum. After some trials, with the initial vector $\boldsymbol{p}^{(0)}$ given above, we found that a perturbation for each design parameter of 2% of its nominal value leads to an acceptable solutions. Its outcome is plotted in figure 4.1.

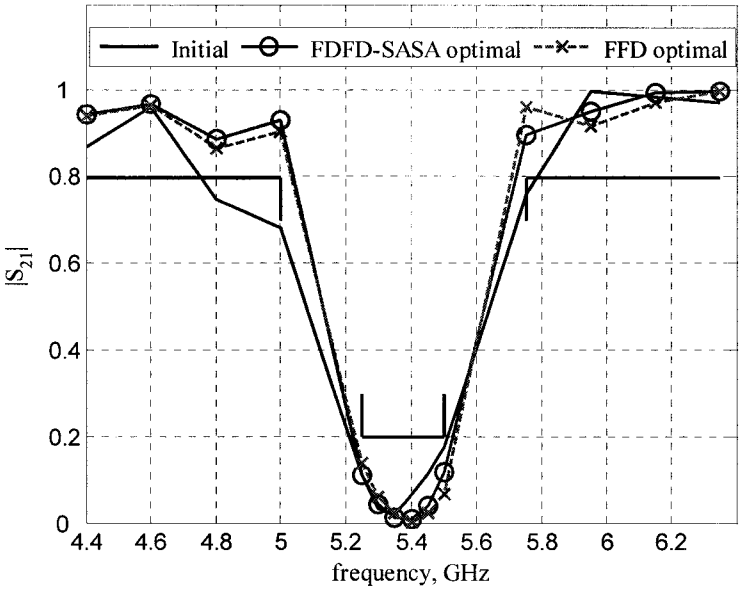

Figure 4.1 Insertion loss of the bandstop filter before and after optimization with FDFD-SASA Jacobians and with FFD Jacobians.

Both optimization processes use the same termination criteria: $\Delta_F^{(k)} =$

$\| F^{(k+1)} - F^{(k)} \| \leq \varepsilon$ or $\Delta_{\boldsymbol{p}}^{(k)} = \| \boldsymbol{p}^{(k+1)} - \boldsymbol{p}^{(k)} \| / \| \boldsymbol{p}^{(k)} \| \leq 0.001$, where $\varepsilon = 0.005$ is the convergence error of the mesh refinement in Ansoft HFSS. The two optimal designs are listed in Table 4.1. Figure 4.2 shows the evolution of the objective functions versus the iterations. It is clear that the two optimization processes are different despite the identical initial point. This is due to the differences in the Jacobians computed via FDFD-SASA and FFD.

TABLE 4.1
OPTIMAL DESIGNS USING FDFD-SASA AND FFD JACOBIANS

all in mm	*t*	*r*	*s*
FDFD-SASA	3.68	3.86	19.79
FFD	4.30	2.74	19.60

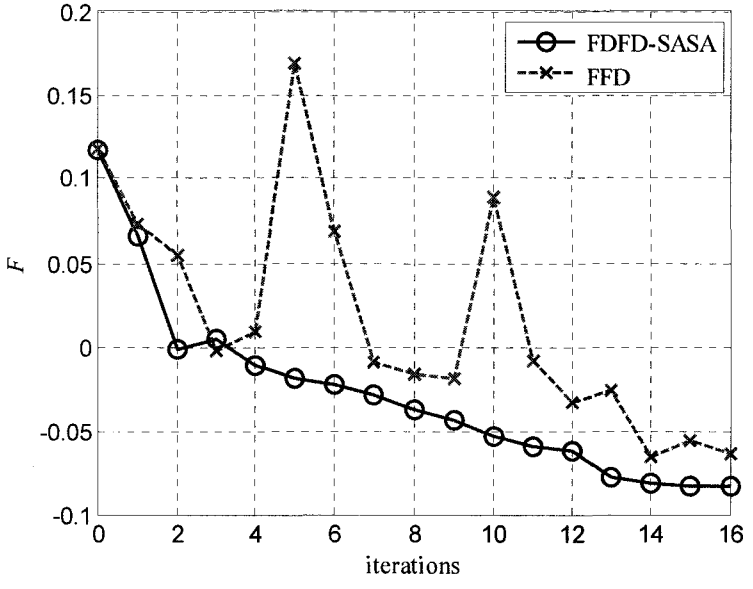

Figure 4.2 The evolution of the objective functions vs. iterations in the optimization of the bandstop filter.

TABLE 4.2
NUMBER OF ITERATIONS AND TIME COMPARISON WITH FDFD-SASA JABOBIANS AND FFD JACOBIANS

Method	FDFD-SASA	FFD
Optimization Iterations	17	17
Calls for EM Simulation	17	68
Response Computation (s)	7803	7803
Jacobian Estimation (s)	7.65	23409

The time required by the FDFD-SASA to compute the Jacobian is about 0.45 s. At the same time, one HFSS frequency sweep takes about 459 s, which results in a computational overhead of 1377 s $(3\times 459\ \text{s})$ for the Jacobian calculation via response-level FFD. These times vary slightly from iteration to iteration and the above values are average. Table 4.2 shows the comparison of the computational overhead of the FDFD-SASA and the FFD. Our method offers more than 3 orders of magnitude time reduction.

To illustrate the serious problem arising from the inaccuracy of the FFD Jacobians, we briefly note that an attempt to optimize the filter starting from $\boldsymbol{p}^{(0)} = [7.5\ 1.5\ 13.5]^T$ mm with the same 2% parameter perturbation failed after 9 iterations with $F = 0.2330$. In contrast, the FDFD-SASSA optimization from this starting point was successful. After 20 iterations, it achieves $F = -0.0677$.

4.3.2 Dielectric-resonator antenna

The dielectric-resonator antenna is shown in figure 3.24. The design specifications are

$$\begin{aligned} |S_{11}| &\geq 0.65 \text{ for } 2.0 \leq f \leq 2.4 \text{ GHz} \\ |S_{11}| &\leq 0.2 \text{ for } 2.82 \leq f \leq 2.98 \text{ GHz} \\ |S_{11}| &\geq 0.65 \text{ for } 3.4 \leq f \leq 3.8 \text{ GHz.} \end{aligned} \tag{4.3}$$

In this example, two optimization procedures are carried out: one with the three shape parameters a, b, and c of the dielectric resonator; and the second one with a, b, c, and the shape parameter l_a of the aperture.

In the three-variable optimization problem, the initial design is $\boldsymbol{p}^{(0)} = [21\ 25\ 13]^T$ mm. A perturbation of $\Delta \boldsymbol{p}_{\text{FFD}} = [0.04a\ 0.04b\ 0.05c]^T$ is utilized to compute the FFD Jacobians at each iteration.

In the four-variable optimization problem, the initial design is $\boldsymbol{p}^{(0)} = [21\ 25\ 13\ 18.5]^T$ mm. A perturbation of $\Delta \boldsymbol{p}_{\text{FFD}} = [0.04a\ 0.04b\ 0.05c\ 0.05l_a]^T$ is utilized to compute the FFD Jacobians at each iteration.

In both optimization problems, the initial trust region is set as $r^{(0)} = 0.1 \| \boldsymbol{p}^{(0)} \|$. The upper bound value for the design parameters is $1.5\boldsymbol{p}^{(0)}$, and the lower one is $0.5\boldsymbol{p}^{(0)}$. The termination criteria are: $\Delta_F^{(k)} = \| F^{(k+1)} - F^{(k)} \| \leq \varepsilon$ or $\Delta_{\boldsymbol{p}}^{(k)} = \| \boldsymbol{p}^{(k+1)} - \boldsymbol{p}^{(k)} \| / \| \boldsymbol{p}^{(k)} \| \leq 0.0125$, where $\varepsilon = 0.01$ is the convergence error of the mesh refinement in Ansoft HFSS [9]. The central-node grid steps Δx, Δy, Δz of the FDFD-SASA are roughly equal to the length of the FEM edge along the corresponding dimension in the computational domain.

Figure 4.3 plots the return loss of the initial design and the two optimal designs. Figure 4.4 shows the evolution of the objective functions versus iterations. The results in figures 3.3 and 3.4 are for the three-variable optimization problem. The results for the four-variable problem are plotted in figures 4.5 and 4.6. Tables 4.3 and 4.4 list the two optimal designs and the comparison of the computational overhead of the FDFD-SASA and the FFD sensitivity analysis for the three-variable problem. The respective results for the four-variable problem are shown in tables 4.5 and 4.6.

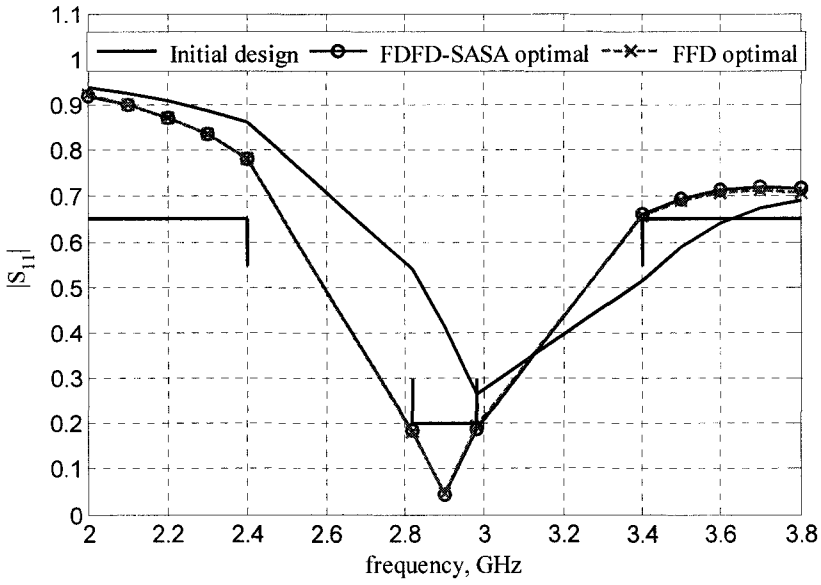

Figure 4.3 Return loss of the dielectric-resonator antenna (3 parameters) before and after optimization with FDFD-SASA Jacobians and with FFD Jacobians.

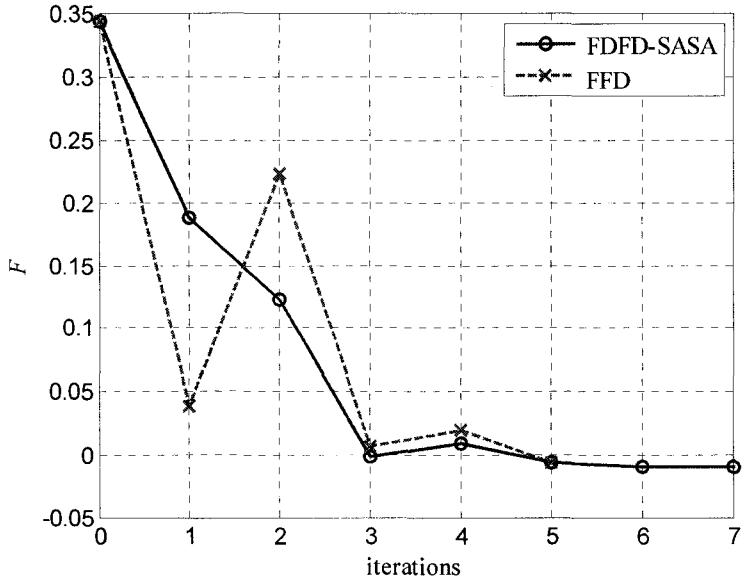

Figure 4.4 The evolution of the objective functions vs. iterations in the optimization of the dielectric-resonator antenna (3 parameters).

TABLE 4.3
OPTIMAL DESIGNs USING FDFD-SASA AND FFD JACOBIANS (3 PARAMETERS)

all in mm	*a*	*b*	*c*
FDFD-SASA	27.55	23.52	12.06
FFD	23.63	24.03	13.97

TABLE 4.4
NUMBER OF ITERATIONS AND TIME COMPARISON WITH FDFD-SASA JABOBIANS AND FFD JACOBIANS (3 PARAMETERS)

Method	FDFD-SASA	FFD
Optimization Iterations	8	6
Calls for EM Simulation	8	24
Response Computation (s)	1760	1320
Jacobian Estimation (s)	0.13	3960

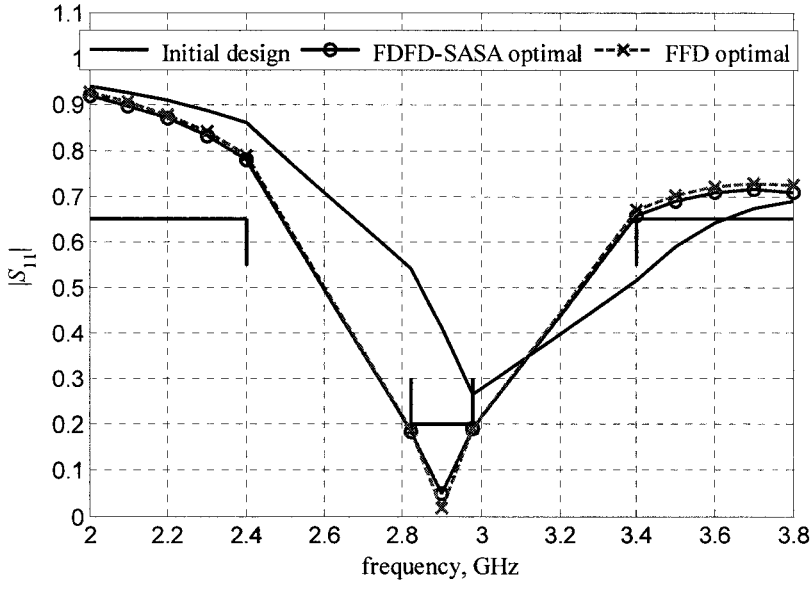

Figure 4.5 Return loss of the dielectric-resonator antenna (4 parameters) before and after optimization with FDFD-SASA Jacobians and with FFD Jacobians.

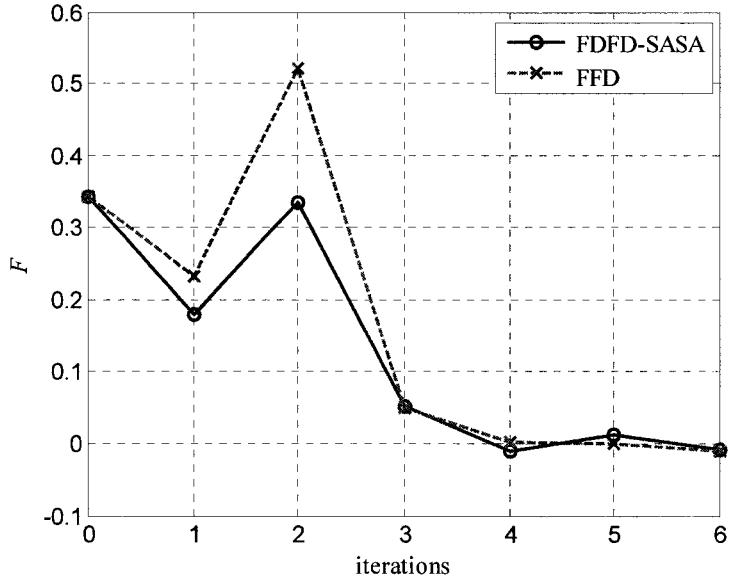

Figure 4.6 The evolution of the objective functions vs. iterations in the optimization of the dielectric-resonator antenna (4 parameters).

TABLE 4.5
OPTIMAL DESIGNs USING FDFD-SASA AND FFD JACOBIANS (4 PARAMETERS)

all in mm	a	b	c	l_a
FDFD-SASA	23.91	25.10	13.43	18.47
FFD	23.87	25.06	13.48	18.08

TABLE 4.6
NUMBER OF ITERATIONS AND TIME COMPARISON WITH FDFD-SASA JABOBIANS AND FFD JACOBIANS (4 PARAMETERS)

Method	FDFD-SASA	FFD
Optimization Iterations	7	7
Calls for EM Simulation	7	35
Response Computation (s)	1540	1540
Jacobian Estimation (s)	0.21	6160

Tables 4.4 and 4.6 demonstrate that the FDFD-SASA is much more efficient than the FFD method. Figures 4.4 and 4.6 show that the convergence result with the FDFD-SASA Jacobians is better than that with the FFD Jacobians, which verifies the reliability of the FDFD-SASA Jacobians again.

4.4 References

[1] D. Li, *Sensitivity Analysis with Finite-element Method for Microwave Design and Optimization*, M.A.Sc. Thesis, Department of Electrical and Computer Engineering, McMaster University, Hamilton, ON, Canada, Jun., 2006.

[2] A. D. Belegundu and T. R. Chandrupatla, *Optimization Concepts and Applications in Engineering Optimization.* Upper Saddle River, NJ: Prentice Hall, 1999, pp. 56-91, 259-278.

[3] J. Robinson and Y. Rahmat-Samii, "Particle swarm optimization in electromagnetics," *IEEE Trans. Antennas Propagation*, vol. 52, pp. 397-407, Feb. 2004.

[4] J. E. Rayas-Sanchez, "EM-based optimization of microwave circuits using artificial neural networks: the state-of-the-art," *IEEE Trans. Microwave Theory Tech.*, vol. 52, pp. 420-435, Jan. 2004.

[5] D. Li, J. Zhu, N.K. Nikolova, M.H. Bakr, and J.W. Bandler, "Electromagnetic optimization using sensitivity analysis in the frequency domain," *IET Proc. Microwaves, Antennas & Propagation*, vol. 1, pp. 852-859, Aug. 2007.

[6] X. Zhu, A. Hasib, N.K. Nikolova, and M.H. Bakr, "Efficient electromagnetic optimization using self-adjoint Jacobian computation based on a central-node FDFD method," *IEEE MTT-S Int. Microwave Symposium*, pp. 979-982, Jun. 2008.

[7] J. W. Bandler, W. Kellermann and K. Madsen, "A superlinearly convergent minimax algorithm for microwave circuit design," *IEEE Trans. Microwave Theory Tech.*, vol. MTT-33, pp. 1519-1630, Dec. 1985.

[8] Ansoft HFSS ver. 10, Ansoft Corporation, 225 West Station Square Drive, Suite 200, Pittsburgh, PA 15219, USA, 2006, www.ansoft.com.

[9] Ansoft HFSS ver. 11, Ansoft Corporation, 225 West Station Square Drive, Suite 200, Pittsburgh, PA 15219, USA, 2007, www.ansoft.com.

Chapter 5

CONCLUSIONS

In this thesis, a self-adjoint sensitivity analysis (SASA) algorithm based on the system equations of the finite-difference frequency-domain (FDFD) method is proposed. This new approach is referred to as the FDFD-SASA. We validate the FDFD-SASA in the design optimization of two microwave devices: an *H*-plane dielectric-resonator filter and a dielectric-resonator antenna.

The FDFD-SASA produces the response information and the gradients with respect to all designable parameters after one system analysis only. It is much more efficient than the finite-difference (FD) approximation method at the response level. Besides, the FDFD-SASA Jacobian computation is completely independent of the simulator's grid, discretization method and system equations. It relies on its own finite-difference grid and a sensitivity formula based on the FDFD equation for the electric field. It operates as a post-process for commercial simulators based on volumetric partial differential equations (PDE).

Chapter 2 outlines the theory of the adjoint variable method (AVM) in the

frequency domain. Both the exact and the approximate AVM are discussed. A computational overhead comparison between the AVM and the FD method is presented. A brief introduction to the SASA based on the finite-element method (FEM) is also given. The implementations of the AVM and the SASA are discussed.

Chapter 3 investigates our new frequency-domain sensitivity analysis approach, the FDFD-SASA. It has the same high efficiency as the SASA but eliminates the requirement to access the system matrix generated by the simulator. Compared to Yee's grid, the application of the central-node finite-difference grid not only improves the accuracy of the derivative calculations but also significantly simplifies the implementation in the case of shape parameters of metallic objects. The implementations of the FDFD-SASA for dielectric structures, metallic structures, and infinitesimally thin metallic structures are discussed. Validation examples are also presented.

Chapter 4 applies the FDFD-SASA to microwave design optimization. We compare the convergence and the time requirements of two independent gradient-based optimization processes where we use two different methods to compute the response gradient—the FDFD-SASA and the FD method. The numerical results demonstrate that the optimization process with the FDFD-SASA Jacobians has better convergence and is overall much faster than the optimization process with the FD Jacobians.

From the experience and knowledge gained in the above work, the

following topics for further research are suggested.

1) The implementations of the FDFD-SASA to magnetic structures and anisotropic structures.
2) The implementations of the FDFD-SASA with other frequency-domain volumetric PDE-based simulators.
3) The development of a practical SASA algorithm suitable for surface integral-equation simulators, e.g., simulators based on the method of moments such as Sonnet ***em*** [1], FEKO [2], etc.

References

[1] ***em***, Sonnet Software Inc., 100 Elwood Davis Road, North Syracuse, NY 13212, USA, www.sonnetusa.com.

[2] FEKO, EM Software & Systems-S.A. (Pty) Ltd., Box 1354, Stellenbosch, 7599, South Africa, www.feko.info.

COMPLETE REFERENCE LIST

Chapter 1

[1] D. G. Cacuci, *Sensitivity & Uncertainty Analysis, Volume 1: Theory*. Boca Raton, FL: Chaman & Hall/CRC, 2003.

[2] A. D. Belegundu and T. R. Chandrupatla, *Optimization Concepts and Applications in Engineering*. Upper Saddle River, NJ: Prentice-Hall, 1999.

[3] E. J. Haug, K. K. Choi, and V. Komkov, *Design Sensitivity Analysis of Structural Systems*. Orlando, FL: Academic, 1986.

[4] S. W. Director and R. A. Roher, "The generalized adjoint network and network sensitivities," *IEEE Trans. Circuit Theory*, vol. CT-16, pp. 318-323, Aug. 1969.

[5] S. W. Director and R. A. Rohrer, "Automated network design—The frequency-domain case," *IEEE Trans. Circuit Theory,* vol. CT-16, pp. 330-337, Aug. 1969.

[6] B. D. H. Tellegen, "A general network theorem with applications," *Philips Res. Rep.*, vol. 7, pp. 259-269, 1952.

[7] P. Penfield, Jr., R. Spence, and S. Duinker, "A generalized form of Tellegen's theorem," *IEEE Trans. Circuit Theory*, vol. CT-17, pp. 302-305, Aug. 1970.

[8] M. H. Bakr, N. K. Nikolova, "An adjoint variable method for time domain TLM with wide-band Johns matrix boundaries," *IEEE Trans. Microwave Theory Tech.*, vol. 52, pp. 678-685, Feb. 2004.

[9] N. K. Nikolova, H. W. Tam, M. H. Bakr, "Sensitivity analysis with the FDTD method on structured grids," *IEEE Trans. Microwave Theory Tech.*, vol. 52, pp. 1207-1216, Apr. 2004.

[10] M. H. Bakr and N. K. Nikolova, "An adjoint variable method for frequency domain TLM problems with conducting boundaries," *IEEE Microwave and Wireless Components Letters*, vol. 13, pp. 408-410, Sep. 2003.

[11] S. M. Ali, N. K. Nikolova, and M. H. Bakr, "Central adjoint variable method for sensitivity analysis with structured grid electromanetic solvers," *IEEE Trans. Magnetics,* vol. 40, pp. 1969-1971, Jul. 2004.

[12] H. Akel and J. P. Webb, "Design sensitivities for scattering-matrix calculation with tetrahedral edge elements," *IEEE Trans. Magnetics*, vol. 36, pp. 1043-1046, Jul. 2000.

[13] N. K. Nikolova, J. Zhu, D. Li, M. Bakr, and J. Bandler, "Sensitivities of network parameters with electromagnetic frequency domain simulators," *IEEE Trans. Microwave Theory Tech.*, vol. 54, pp. 670-681, Feb. 2006.

[14] N. K. Nikolova, Ying Li, Yan Li, and M. H. Bakr, "Sensitivity analysis of scattering parameters with electromagnetic time-domain simulators," *IEEE Trans. Microwave Theory Tech.*, vol. 54, pp. 1589-1610, Apr. 2006.

[15] X. Zhu, A. Hasib, and N. K. Nikolova, "Electromagnetic sensitivity analysis of scattering parameters based on the FDFD method," *Int. Symp. on Signals, Systems, and Electronics (ISSSE 2007)*, pp. 165-168, Jul.-Aug. 2007.

[16] N. K. Nikolova, A. Hasib, and X. Zhu, "Independent sensitivity solver based on the frequency domain finite difference method," *The 24th Int. Review of Progress in Applied Computational Electromagnetics (ACES 2008)*, pp. 1024-1029, Mar.-Apr. 2008.

[17] Ansoft HFSS ver. 10, Ansoft Corporation, 225 West Station Square Drive, Suite 200, Pittsburgh, PA 15219, USA, 2006, www.ansoft.com.

[18] Ansoft HFSS ver. 11, Ansoft Corporation, 225 West Station Square Drive, Suite 200, Pittsburgh, PA 15219, USA, 2007, www.ansoft.com.

[19] X. Zhu, A. Hasib, N.K. Nikolova, and M.H. Bakr, "Efficient electromagnetic optimization using self-adjoint Jacobian computation based on a central-node FDFD method," *IEEE MTT-S Int. Microwave Symposium*, pp. 979-982, Jun. 2008.

Chapter 2

[1] N. K. Nikolova, H. W. Tam, M. H. Bakr, "Sensitivity analysis with the FDTD method on structured grids," *IEEE Trans. Microwave Theory Tech.*, vol. 52, pp. 1207-1216, Apr. 2004.

[2] N. K. Nikolova, J. Zhu, D. Li, M. Bakr, and J. Bandler, "Sensitivities of network parameters with electromagnetic frequency domain simulators," *IEEE Trans. Microwave Theory Tech.* vol. 54, pp. 670-681, Feb. 2006.

[3] N. K. Nikolova, Ying Li, Yan Li, and M. H. Bakr, "Sensitivity analysis of scattering parameters with electromagnetic time-domain simulators," *IEEE Trans. Microwave Theory Tech.*, vol. 54, pp. 1589-1610, Apr. 2006.

[4] N. K. Nikolova, J. W. Bandler, and M. H. Bakr, "Adjoint techniques for sensitivity analysis in high-frequency structure CAD," *IEEE Trans. Microwave Theory Tech.*, vol. 52, pp. 403-419, Jan. 2004.

[5] J. Jin, *The Finite Element Method in Electromagnetics*, 2nd ed. New York: John Wiley & Sons, 2002.

[6] S. M. Ali, N. K. Nikolova, and M. H. Bakr, "Recent advances in sensitivity analysis with frequency-domain full-wave EM solvers," *Applied Computational Electromagnetics Society Journal.*, vol. 19, pp. 147-154, Nov. 2004

[7] E. J. Haug, K. K. Choi, and V. Komkov, *Design Sensitivity Analysis of Structural Systems.* Orlando, FL: Academic, 1986.

[8] M. D. Greenberg, *Advanced Engineering Mathematics*. Upper Saddle River, NJ: Prentice Hall, 1998, pp. 605.

[9] M. H. Bakr and N. K. Nikolova, "An adjoint variable method for time domain TLM with fixed structured grids," *IEEE Trans. Microwave Theory Tech.*, vol. 52, pp. 554-559, Feb. 2004.

[10] R. F. Harrington, *Time-Harmonic Electromagnetic Fields*. New York: McGraw-Hill book company, Inc., 1961.

[11] J. L. Volakis, A. Chatterjee, L. C. Kempel, *Finite Element Method for Electromagnetics*, New York: The Institute of Electrical and Electronics Engineers, Inc., 1998.

[12] H. Akel and J. P. Webb, "Design sensitivities for scattering-matrix calculation with tetrahedral edge elements," *IEEE Trans. Magnetics*, vol. 36, pp. 1043-1046, Jul. 2000.

Chapter 3

[1] N. K. Nikolova, J. Zhu, D. Li, M. Bakr, and J. Bandler, "Sensitivities of network parameters with electromagnetic frequency domain simulators," *IEEE Trans. Microwave Theory Tech.*, vol. 54, pp. 670-681, Feb. 2006.

[2] X. Zhu, A. Hasib, and N. K. Nikolova, "Electromagnetic sensitivity analysis of scattering parameters based on the FDFD method," *Int. Symp.*

on Signals, Systems, and Electronics (ISSSE 2007), pp. 165-168, Jul.-Aug. 2007.

[3] N. K. Nikolova, A. Hasib, and X. Zhu, "Independent sensitivity solver based on the frequency domain finite difference method," *The 24th Int. Review of Progress in Applied Computational Electromagnetics (ACES 2008)*, pp. 1024-1029, Mar.-Apr. 2008.

[4] N. K. Nikolova, H. W. Tam, M. H. Bakr, "Sensitivity analysis with the FDTD method on structured grids," *IEEE Trans. Microwave Theory Tech.*, vol. 52, pp. 1207-1216, Apr. 2004.

[5] N. K. Nikolova, Ying Li, Yan Li, and M. H. Bakr, "Sensitivity analysis of scattering parameters with electromagnetic time-domain simulators," *IEEE Trans. Microwave Theory Tech.*, vol. 54, pp. 1589-1610, Apr. 2006.

[6] Ansoft HFSS ver. 10, Ansoft Corporation, 225 West Station Square Drive, Suite 200, Pittsburgh, PA 15219, USA, 2006, www.ansoft.com.

[7] Ansoft HFSS ver. 11, Ansoft Corporation, 225 West Station Square Drive, Suite 200, Pittsburgh, PA 15219, USA, 2007, www.ansoft.com.

[8] M. H. Bakr and N. K. Nikolova, "An adjoint variable method for frequency domain TLM problems with conducting boundaries," *IEEE Microwave and Wireless Components Letters,* vol. 13, pp. 408-410, Nov. 2003.

[9] Y. Song, Ying Li, N. K. Nikolova, and M.H. Bakr, "Self-adjoint sensitivity analysis of lossy dielectric structures with electromagnetic

time-domain simulators," *Int. J. of Numerical Modelling: Electronic Networks, Devices and Fields,* vol. 21, pp. 117-132, Oct. 2007.

[10] Y. Song and N.K. Nikolova, "Central-node approach for accurate self-adjoint sensitivity analysis of dielectric structures," *IEEE MTT-S Int. Microwave Symposium*, pp. 895-898, Jun. 2007.

[11] L. Minakova and L. Rud, "Spectral approach to the synthesis of the waveguide bandstop filters based on dielectric rectangular posts," *Int. Conference on Mathematical Methods in Electromagnetic Theory MMET*, pp. 479-481, Sep. 2000.

[12] D. Yau and N. V. Shuley, "A moment method analysis of an aperture coupled rectangular dielectric resonator antenna," *IEEE AP-S/URSI Int. Antennas Propagation Symposium*, vol. 2, pp. 858-861, Jul. 1999.

[13] A. Hasib, *Sensitivity Analysis for Design Optimization of Metallic Microwave Structures with the Finite-difference Frequency-domain Method*, M.A.Sc. Thesis, Department of Electrical and Computer Engineering, McMaster University, Hamilton, ON, Canada, Apr. 2008.

Chapter 4

[1] D. Li, *Sensitivity Analysis with Finite-element Method for Microwave Design and Optimization*, M.A.Sc. Thesis, Department of Electrical and Computer Engineering, McMaster University, Hamilton, ON, Canada, Jun., 2006.

[2] A. D. Belegundu and T. R. Chandrupatla, *Optimization Concepts and Applications in Engineering Optimization*. Upper Saddle River, NJ: Prentice Hall, 1999, pp. 56-91, 259-278.

[3] J. Robinson and Y. Rahmat-Samii, "Particle swarm optimization in electromagnetics," *IEEE Trans. Antennas Propagation*, vol. 52, pp. 397-407, Feb. 2004.

[4] J. E. Rayas-Sanchez, "EM-based optimization of microwave circuits using artificial neural networks: the state-of-the-art," *IEEE Trans. Microwave Theory Tech.*, vol. 52, pp. 420-435, Jan. 2004.

[5] D. Li, J. Zhu, N.K. Nikolova, M.H. Bakr, and J.W. Bandler, "Electromagnetic optimization using sensitivity analysis in the frequency domain," *IET Proc. Microwaves, Antennas & Propagation*, vol. 1, pp. 852-859, Aug. 2007.

[6] X. Zhu, A. Hasib, N.K. Nikolova, and M.H. Bakr, "Efficient electromagnetic optimization using self-adjoint Jacobian computation based on a central-node FDFD method," *IEEE MTT-S Int. Microwave Symposium*, pp. 979-982, Jun. 2008.

[7] J. W. Bandler, W. Kellermann and K. Madsen, "A superlinearly convergent minimax algorithm for microwave circuit design," *IEEE Trans. Microwave Theory Tech.*, vol. MTT-33, pp. 1519-1630, Dec. 1985.

[8] Ansoft HFSS ver. 10, Ansoft Corporation, 225 West Station Square Drive, Suite 200, Pittsburgh, PA 15219, USA, 2006, www.ansoft.com.

[9] Ansoft HFSS ver. 11, Ansoft Corporation, 225 West Station Square Drive, Suite 200, Pittsburgh, PA 15219, USA, 2007, www.ansoft.com.

Chapter 5

[1] ***em***, Sonnet Software Inc., 100 Elwood Davis Road, North Syracuse, NY 13212, USA, www.sonnetusa.com.

[2] FEKO, EM Software & Systems-S.A. (Pty) Ltd., Box 1354, Stellenbosch, 7599, South Africa, www.feko.info.